Applied
Magnetic Resonance

CrossMark

The Current State of Measuring Bimolecular Spin Exchange Rates by the EPR Spectral Manifestations of the Exchange and Dipole–Dipole Interactions in Dilute Solutions of Nitroxide Free Radicals with Proton Hyperfine Structure

Barney L. Bales[1] · M. M. Bakirov[2] ·
R. T. Galeev[2] · I. A. Kirilyuk[3] · A. I. Kokorin[4] ·
K. M. Salikhov[2]

Abstract Experimental studies of 4-hydroxy-2,2,6,6-tetramethylpiperidine 1-oxyl (Tempol) in 60 wt% aqueous glycerol were carried out for temperatures from 273 to 340 K. Selective isotope substitution allowed comparisons between the experimental spectral manifestations of spin exchange and dipole–dipole interactions for protonated, deuterated, ^{15}N, and ^{14}N Tempol. Theoretical spectra were computed from a rigorous theory specifically formulated to include proton hyperfine interactions over a wide range of spin exchange and dipole–dipole interactions to compare with the experimental data. For spin exchange and dipole–dipole interactions small compared with the proton hyperfine coupling constant, spectra were calculated with perturbation theory to gain insight into the behavior of individual proton lines. The theoretical and experimental spectra were analyzed by least-squares fitting to Voigt shapes or by a new two-point method. For most accessible experimental designs, the comparisons are rather good; however, for an experiment constrained to low concentrations and high viscosities, the methods are less accurate.

✉ Barney L. Bales
  barney.bales@csun.edu

[1] Department of Physics and Astronomy, The Center for Biological Physic, California State University at Northridge, Northridge, CA 91330, USA

[2] Zavoisky Physical-Technical Institute, Russian Academy of Sciences, Sibirsky trakt 10/7, Kazan 420029, Russian Federation

[3] Novosibirsk Institute of Organic Chemistry of the Siberian Branch of the Russian Academy of Sciences, Novosibirsk, Russian Federation

[4] Semenov Institute of Chemical Physics of the Russian Academy of Sciences, Moscow, Russian Federation

1 Introduction

Electron paramagnetic resonance (EPR) of free radicals in solution often show resolved hyperfine structure (hfs) due to the coupling of the unpaired electron with magnetic nuclei in the same molecule. See Table 1 for a list of definitions, abbreviations and acronyms. In 1959, a remarkable temperature dependence of this resolution, which appeared and then disappeared upon raising the temperature, [1] led Pake and Tuttle [2] to suggest that Heisenberg spin exchange (HSE) was responsible for the high-temperature behavior. One year later, Kivelson [3] cited Pake and Tuttle's "ingenious explanation of the phenomenon" as his reason to "develop the exchange effects between free radicals in liquids in somewhat more detail." His theory was able to predict the effects of HSE in two limits: (1) slow HSE, when the spin exchange frequency, ω_{ex}, is much less than the hyperfine spacing or (2) fast HSE, in the other extreme. For slow HSE, the hyperfine lines

Table 1 Definitions, abbreviations and acronyms

hfs	Hyperfine structure
HSE, DD	Heisenberg spin exchange and dipole–dipole interactions, respectively
IHB	Inhomogeneous broadening of the nitrogen hyperfine lines, principally due to hfs for protons or deuterons, but also due to magnetic field modulation
Manifold	Superposition of proton or deuteron spin modes corresponding to each nitrogen nuclear quantum number
$C \rightarrow 0$	Indicates absence of HSE or DD
Dark zone	The region of HSE or DD where the hfs disappears; i.e., where $VC \approx$ hyperfine spacing. For nitroxides, there are two such zones with $VC \approx a$, the proton dark zone, and $VC \approx A_0$ the nitrogen dark zone
Absorption	The component of an absorption spectrum with a first-derivative shape given by Eq. (11)
Dispersion	The component of an absorption spectrum with a first-derivative shape induced by HSE and/or DD that has the mathematical form of a dispersion given by Eq. (12). This signal is distinguished from the in-phase signal due to a slight mismatch of the microwave cavity by calling the latter the instrumental dispersion
Voigt(s), Lorentzian(s), Gaussian(s)	First-derivative Voigt, Lorentzian, or Gaussian line shape functions, respectively, used as adjectives to modify dispersion or absorption. For example, we refer to a Voigt dispersion or a Lorentzian absorption, etc.
$\Delta H_{ppM}^{G(Voigt)}$, $\Delta H_{ppM}^{L(Voigt)}$	The Gaussian and Lorentzian components of a Voigt manifold
Fit	Verb, performing a least-square fit. Noun, the result of the fit
HVL, LVL	The high- or low- viscosity limit of the spectral densities of the correlation functions for DD, respectively
Nitroxide	Nitroxide free radicals
Partially resolved spectrum	A spectrum such as that in Fig. 8b. A subjective term, quantified by the Voigt parameter. See text
Spectrum showing incipient resolution	A spectrum such as that in Fig. 8c. A subjective term, quantified by the Voigt parameter. See text

broaden and shift toward one another, the less intense lines broadening the most. For fast HSE, the hyperfine pattern merges into one line and narrows. The intermediate region, where ω_{ex} is comparable to the spacing was not accessible. We call this intermediate region the "dark region." We write $\omega_{ex} = K_{ex}C$, where K_{ex} is the rate constant for HSE and C is the radical concentration in units mol/L.

Two years after Kivelson's work, Currin [4] developed a rigorous theory describing the effects of HSE in a single equation that was valid over the entire range of $K_{ex}C$ from good resolution to extreme narrowing. He reproduced Kivelson's results for slow and fast HSE, and could predict the resulting spectra in the dark region, but not an account of what happened to the hyperfine lines that had merged into a single line and had collapsed into a single narrow line. In modern times, we refer to these "lines" as spin modes recognizing that each mode is a collective state not representing a particular spin [5].

Over the next few years after Currin's paper, there was intense activity by some of the best minds in EPR as summarized in Ref. [6] culminating in a monograph in English in 1980 [7] dedicated entirely to HSE. Studying HSE by EPR is a powerful method to study bi-molecular encounters and re-encounters. Its power derives from the fact that the interaction is very short range, occurring only during the short time in which the overlap of unpaired spin orbitals between the two colliding radicals is significant.

A very large set of combinations of various types of paramagnetic particles were utilized in experiments which are summarized in the monograph; [7] here, we restrict our attention to nitroxide free radicals (nitroxides) in dilute solution focusing on methods to analyze the spectra. For the wealth of uses of HSE between nitroxides to study many problems in physics, chemistry, and biology, consult the monograph [7], an excellent entry into the literature. Later, information is available in the series of monographs edited by Berliner [8–10] and references therein which include monographs and textbooks. Updates to 2009 may be found in Refs. [6, 11] and references therein.

It has been appreciated for many years that to study bimolecular collisions of nitroxide free radicals in solution using HSE, the effects of dipole–dipole interactions (DD) must be taken into account. Early efforts to separate HSE and DD employed a hydrodynamic model to model the temperature dependence of the line widths; however, these were not very successful [12]. In fact, Berner and Kivelson [12] showed that those methods were unlikely to successfully effect the separation because the line width did not show a hydrodynamic behavior.

An important development ensued in 1976 when one of the authors (Salikhov) of the monograph [7] derived for each spin mode, in the slow-HSE limit, expressions of the form of a Lorentzian absorption plus an additional term antisymmetric in the non-derivative presentation of the spectrum. This additional term was not employed in analyzing experimental spectra until 21 years later when Bales and Peric [6] recognized that it had the mathematical form of a dispersion signal, and coined the term spin-exchange-induced dispersion [6]. These authors rewrote Salikov's expressions in a form applicable to experimental spectra and incorporated them into a fitting routine to separately determine the absorptions and dispersions and showed that values of K_{ex} could be determined from the dispersions with a precision

that rivaled those found from the line width. In that work [6], Fremy's salt was studied at high temperature; thus, DD did not complicate the analysis.

An interesting historical fact seems to have escaped attention. Currin [4] found the dispersion term in the slow-HSE limit; however, because the focus at the time and for many years afterward was on the line width, he dismissed it saying "The second term leads to an antisymmetric contribution of order $K_{ex}C$ to each hyperfine component and will be of no further interest to us" [4]. Ironically, in recent work [5, 13] and in this paper, we find that the dispersion component plays a dominate role in the dark zones and is like a mean mother, indispensable but difficult.

Bales et al. [11], fitting experimental spectra with an absorption/dispersion line shape supposing that HSE introduced the dispersion and DD did not, could separate HSE and DD at a single temperature leading to results that were reasonable: HSE increased with T/η, where T is the temperature and η the shear viscosity of the solution, while DD decreased. Nevertheless, there was an unexplained negative dispersion signal at low values of T/η [11]. This led Salikhov to report in 2010 [14] that work in 1976 [15] (see Ch. 4, Sect. 1, Eqs. (4.20, 4.21) had already predicted that DD produces a dispersion term, but with a sign opposite to that for HSE. This fact had escaped the attention of workers in the field. It had also been overlooked in previous theories (see, e.g., [16], Ch. VIII). The peculiar opposite signs result from the fact that the quantum coherence has a 180° phase shift when it is transferred from one paramagnetic particle to another by DD while there is no shift for HSE. The 2010 paper [14] worked out explicitly the expressions to describe the manifestations of HSE and DD for nitroxides that showed significant hyperfine coupling to no nuclei other than nitrogen. However, there are no such nitroxides except for Fremy's salt. Thus, inhomogeneous broadening (IHB) by protons or deuterons, must be taken into account for accurate work. Last year, Salikhov et al. [17] extended the work to nitroxides with a formulation that takes into account patterns of hfs due to other nuclei.

Employing a more complete theory of HSE and DD wherein negative dispersions occurred naturally, ^{14}N nitroxide data considered in 2009 were reanalyzed in 2014 [18]. Furthermore, in the same paper [18], similar studies of ^{15}N were used to compare the results of the two isotopes and to introduce a new approach to separate HSE and DD: the relative broadening constant method (RBCM). The three methods, using the dispersion component of the two isotopes and the RBCM were in general agreement, although there were systematic differences, seemingly outside of experimental uncertainty. The nitroxides employed in 2014 were per-deuterated, mitigating but not eliminating the need to consider the effect of the deuteron hfs.

Actually, ^{14}N nitroxide spectra undergoing HSE were analyzed [19] 33 years ago by showing that the line shape was adequately described by a Voigt and assuming that the broadening of the Lorentzian component was equal to $4K_{ex}C/3\sqrt{3}\gamma$. The problem of the asymmetric low- and high-field lines, now known to be due to an admixture of dispersion and absorption components, was avoided by working with the central line of ^{14}N nitroxide. Last year's paper called into question using a Voigt approximation for interacting spins [17] and developed approximate methods to analyze the data avoiding that assumption. Here, we investigate carefully the legitimacy of the 1984 approach presented as assumption 1 below [19].

Unlike our posture in the past to view IHB as a problem to be overcome, we now view the proton structure as a resource allowing us a thus far limited view into the proton dark zone. This view can only be as accurate as our ability to find correct Lorentzian line widths and to find separate absorption and dispersion components in the IHB spectra.

The purpose of the present paper is to test the methods used previously [18] by comparing the results from 4-hydroxy-2,2,6,6-tetramethylpiperidine-1-^{15}N-oxyl (15 NH), 4-hydroxy-2,2,6,6-tetramethylpiperidine-d$_{17}$-1-^{15}N-oxyl (15 ND), and 4-hydroxy-2,2,6,6-tetramethylpiperidine 1-oxyl (14 NH). In addition, a new method that does not require non-linear least-squares fitting to separate HSE and DD is applied to experimental data and compared with the fitting methods. The new method [14, 17] requires measurement of two points on each line and is referred to as the "two-point method." The study of this hydrogen bonding spin probe offers a complement to earlier studies [18] of a similar probe with less hydrogen bonding capacity in a similar solvent.

2 Theory

2.1 General Formulation of the Spectral Manifestations of HSE and DD Interactions

Equations (8) and (9) of SBG (2016) give the spectrum of a radical undergoing HSE and/or DD with any set of hyperfine interactions. The equations are rigorous within the restrictions detailed on p. 1101 of Ref. [17] which are likely to be valid for viscosities that may be studied by these methods. Equation (8), while being general and rigorous, is not easily discussed for a general case; thus, instead of reproducing it as derived, we specialize it to nitroxides that are IHB by hyperfine interactions with protons. The hyperfine interactions naturally separate into those for nitrogen and much smaller interactions with protons. To simplify further, we consider N equivalent protons. This applies directly to radicals such as di-*tert*-butylnitroxide and 2,2,6,6-tetramethyl-4-oxopiperidine-1-oxyl and is a good approximation for most nitroxides when the Voigt parameter, $\chi_M < 2$, Eq. (8) below, because all proton patterns yield the same results to the precision detailed in [20]. The advantage of these restrictions is that a concrete, clearer exposition may be presented, maintaining the essential physical content. The spectrum is proportional to the first-derivative of the real part of the following:

$$Y(H) = -\frac{G(H)}{1 + G(H)(K_{ex} + (2I + 1)V_{dd})C}, \tag{1}$$

where

$$G(H) = \sum_{mM} \frac{\rho_{mM}}{-T_{2M}^{-1} - i\gamma(H_{0mM} - MA_0 - (m - N/2)a - H) - C(K_{ex} + W_{dd} + V_{dd})}, \tag{2}$$

where H_{0mM} is the resonance field of the mMth proton line and H is the swept magnetic field. $H_{0mM} = H_0 - MA_0 - ma$, where H_0 is the resonance field of the spectrum. The sum over m extends over all of the proton lines, $m = 0$–N, numbered from low- to high-field in each manifold, I is the nuclear spin of the nitrogen and A_0 and a the nitrogen and proton hyperfine coupling constants for $C \rightarrow 0$, respectively. The sum over M, the nitrogen nuclear quantum number, is over the manifolds $-1/2$ and $+1/2$ for ^{15}N and $+1$, 0, and -1 for ^{14}N. Furthermore, Eq. (2) assumes that, within a given manifold, the Lorentzian line width $\Delta H_{ppM}^L(0) = 2T_{2M}^{-1}/(\gamma\sqrt{3})$ due to relaxation mechanisms other than HSE or DD is the same, independent of m. The statistical weight, ρ_{mM} is given by:

$$\rho_{mM} = \frac{1}{2I+1}\rho_m, \tag{3}$$

where ρ_m is the statistical weight of each proton hyperfine line within a manifold, normalized to unity. For N equivalent protons, ρ_m is given by the following:

$$\rho_m = \frac{1}{2^N}\frac{N!}{(N-m)!m!}. \tag{4}$$

A term describing extra line shifts for HSE due to repeated collisions while the two nitroxides are within a cage [21], has been omitted. To simplify the notation, we denote the low-, central-, and high-field values of M by lf, cf, and hf for ^{14}N and lf and hf for ^{15}N.

The DD rate constants, Eqs. (5) and (6) of Ref. [18] derived from equations on pp. 239–240 of Ref. [14] are as follows:

$$W_{dd} = \kappa^2\left[\frac{3}{8}J^{(2)}(2\omega_0) + \frac{18I+15}{4(2I+1)}J^{(1)}(\omega_0) + \frac{10I+9}{24(2I+1)}J^{(0)}(0)\right]N_A(10^{-3}), \tag{5}$$

$$V_{dd} = -\frac{1}{2I+1}\kappa^2\left[\frac{3}{2}J^{(1)}(\omega_0) + \frac{1}{6}J^{(0)}(0)\right]N_A(10^{-3}), \tag{6}$$

where $\omega_0 = \gamma H_0$ and the microwave frequency, $\omega = \gamma H$. $\kappa^2 = 3\gamma^4 h^2/4$ for electron spins, where γ is the gyromagnetic ratio of the electron, $J^{(n)}(\omega)$ are the spectral densities of the correlation functions for DD, and N_A is Avogadro's number [18]. Spectral densities are usually given in concentration units cm^{-3} [16] and the factor $N_A(10^{-3})$ changes the units to molarity [18].

The rate constants in Eqs. (5) and (6) were calculated in Ref. [14] for nitroxides without protons. The appropriate expressions to calculate DD line widths are developed below. These rate constants may be simplified in two limits: the high-viscosity limit (HVL) where $J^{(2)}(2\omega_0) = 0$ and $J^{(1)}(\omega_0) = 0$ or in the low-viscosity limit (LVL), where $J^{(2)}(2\omega_0): J^{(1)}(\omega_0): J^{(0)}(0) = 4:1:6$. See after Eq. (VIII. 79) of Ref. [16]. Although there is a difference in the HVL and the LVL in principle, in practice, the difference in the parameter that separates HSE and DD broadening is within experimental error. See Fig. 5 of Ref. [18]. Thus, we present the HVL in this paper. See the Supplemental Information of Ref. [18] for the expressions in the LVL. In the HVL,

$$\frac{V_{\mathrm{dd}}}{W_{\mathrm{dd}}} = \frac{-4}{10I + 9}. \tag{7}$$

For $C \to 0$, Eq. (1) yields IHB absorption manifolds that were treated exhaustively in [20] by exploiting the fact that the profiles of complicated hyperfine coupling patterns are nearly Gaussian, therefore, the Voigt line shape accurately models those nitroxides. The Voigt line shape is determined uniquely by the Voigt parameter

$$\chi_M = \Delta H_{\mathrm{pp}M}^{\mathrm{G(Voigt)}} / \Delta H_{\mathrm{pp}M}^{\mathrm{L(Voigt)}}, \tag{8}$$

where for any set of hyperfine coupling constants, a_j with nuclear spin I_j

$$\Delta H_{\mathrm{pp}M}^{\mathrm{G(Voigt)}} = 2\Big[\alpha \sum I_j(I_j + 1)a_j^2/3\Big]^{1/2},$$

where α is a parameter near unity that adjusts the half-height of the pattern to that of the Gaussian, pp. 92–93 of [20]. In the case of nitroxides, considering protons and deuterons, the Voigt approximation is excellent for all of the known proton patterns and for many other fictitious patterns except when a_j for a single proton is much larger than any of the others [20]. For equivalent protons,

$$\Delta H_{\mathrm{pp}M}^{\mathrm{G(Voigt)}} = a\sqrt{\alpha N}, \tag{9}$$

with $\alpha = 1.08$ for $N = 12$.

2.2 Perturbation Theory of HSE and DD

Let us introduce the parameter that characterizes the rate of coherence transfer

$$V = V_{\mathrm{dd}} + V_{\mathrm{ex}}, \tag{10}$$

where $V_{\mathrm{ex}} = K_{\mathrm{ex}}/(2I + 1)$ and V_{dd} is given by Eq. (6). Thus, the "rate" constant of spin coherence transfer is given by $K_{\mathrm{ct}} = (2I + 1)V$.

The spectrum may be represented by the following for any value of V including extreme narrowing of the entire spectrum as follows:

$$Y' = \sum_{m,M}\Big[V_{\mathrm{pp}mM}L_{mM}^{\prime\mathrm{abs}} + V_{\mathrm{disp}mM}L_{mM}^{\prime\mathrm{disp}}\Big], \tag{11}$$

where

$$L_{mM}^{\prime\mathrm{abs}} = \frac{-8\xi_{mM}}{(3 + \xi_{mM}^2)^2}, \tag{12}$$

and

$$L_{mM}^{\prime\mathrm{disp}} = \frac{3(3 - \xi_{mM}^2)}{(3 + \xi_{mM}^2)^2}. \tag{13}$$

$L_{mM}^{\prime\text{abs}}$ is the component with a Lorentzian absorption shape of unit peak-to-peak height and $L_{mM}^{\prime\text{disp}}$ is the component with a Lorentzian dispersion shape of unit maximum intensity, with

$$\xi_{mM} = 2\frac{H - H_{mM}}{\Delta H_{\text{pp}M}^{\text{L}}}, \tag{14}$$

where the line widths, $\Delta H_{\text{pp}M}^{\text{L}}$, are treated in Eqs. (35) and (41) below. The integrated intensity of each proton line is

$$I_{mM} = \frac{\pi}{\sqrt{3}} V_{\text{pp}mM}(\Delta H_{\text{pp}mM}^{\text{L}})^2. \tag{15}$$

For $C \to 0$

$$I_{mM} = \frac{\pi}{\sqrt{3}} V_{\text{pp}mM}(0)(\Delta H_{\text{pp}mM}^{\text{L}}(0))^2.$$

Thus, within each manifold

$$V_{\text{pp}mM} = V_{\text{pp}mM}(0)\left(\frac{\Delta H_{\text{pp}mM}^{\text{L}}(0)}{\Delta H_{\text{pp}mM}^{\text{L}}}\right)^2, \tag{16}$$

where $V_{\text{pp}mM}(0) \propto \rho_{mM}$. The constant of proportionality does not matter in our computations; however, if we wish to display a spectrum with several manifolds, then we must scale manifold M' to manifold M as follows:

$$V_{\text{pp}mM}(0) = V_{\text{pp}mM'}(0)\left(\frac{\Delta H_{\text{pp}mM}^{\text{L}}(0)}{\Delta H_{\text{pp}mM'}^{\text{L}}(0)}\right)^2. \tag{17}$$

The coefficients $V_{\text{pp}mM}$ and $V_{\text{disp}mM}$ are very complicated functions of VC even for two or three lines [5] in the absence of proton lines; however, for $VC \ll \gamma a$, perturbation theory is applicable. See Eq. (2.81), p. 47 above Eq. (2.86), the equations immediately preceding Eq. (2.86) of [7], or the equivalent Eqs. (5)–(20) of Ref. [6] where they are presented in terms of measured quantities.

The resonance field of the mMth line is given by

$$H_{mM} = H_{mM}(0) + \delta H_{mM}, \tag{18}$$

where the line shifts due to HSE are given by Eq. (22) of Ref. [6]; see also Ref. [7]. When generalized to HSE and DD we have

$$\delta H_{mM} = -\rho_{mM}\left(\frac{(2I+1)VC}{\gamma}\right)^2 \sum_{m'M' \neq mM} \frac{\rho_{m'M'}}{H(0)_{mM} - H(0)_{m'M'}}, \tag{19}$$

where the sum is carried out over all hyperfine lines except the one labeled by mM. We see that line shifts are independent of the sign of V.

The relative intensity of the induced dispersion component is given by the following [6, 7]:

$$\frac{V_{\text{disp}mM}}{V_{\text{pp}mM}} = -\frac{8\sqrt{3}}{9} \frac{(2I+1)VC}{\gamma} \sum_{m'M' \neq mM} \frac{\rho_{m'M'}}{H(0)_{mM} - H(0)_{m'M'}}. \tag{20}$$

Denote the sum in Eqs. (19) and (20) as follows:

$$\Sigma_{mM} \equiv \sum_{m'M' \neq mM} \frac{\rho_{m'M'}}{H(0)_{mM} - H(0)_{m'M'}}. \tag{21}$$

For nitroxides, Σ_{mM} divides naturally into interactions between members of different manifolds (inter-manifold) and those within the same manifold (intra-manifold).

2.2.1 Inter-Manifold

To be concrete, let us begin by considering ^{15}N and selecting line m from the lf-manifold. From Eq. (3), $\rho_{m'M'} = \rho_{m'}/(2I+1)$. The denominator of Eq. (21) is the separation between the line m in the lf-manifold and the line m' in the hf-manifold which is given by

$$H(0)_{m\text{lf}} - H(0)_{m'\text{hf}} = -A_0 - a \cdot (m' - m) \tag{22}$$

Expanding in the small parameter a/A_0

$$\Sigma_{m\text{lf}}^{\text{inter}} = \frac{-1}{(2I+1)A_0} \sum_{m'} \rho_{m'} \left[1 - \frac{a}{A_0} \cdot (m' - m) \right], \tag{23}$$

so

$$\Sigma_{m\text{lf}}^{\text{inter}} = \frac{-1}{2A_0} \left(1 + \frac{a}{A_0} [m - m'] \right) \tag{24}$$

because $\sum \rho_{m'} = 1$ where the first moment of m', $m' \equiv \sum m' \rho_{m'}$.

For ^{14}N, the calculation is similar except that $(2I+1) = 3$ and the sum over the cf- and hf-manifolds involves one at spacing A_0 and another at $2A_0$ yielding

$$\Sigma_{m\text{lf}}^{\text{inter}} = \frac{-1}{2A_0} \left(1 + \frac{5a}{6A_0} [m - m'] \right). \tag{25}$$

Equations (24) and (25) may be written for either isotope as follows:

$$\Sigma_{m\text{lf}}^{\text{inter}} = \frac{-1}{2A_0} \left(1 + \frac{(4I+1)}{6I} \frac{a}{A_0} [m - m'] \right). \tag{26}$$

The mean value of $\Sigma_{m\text{lf}}^{\text{inter}}$ over the low-field manifold is given by

$$\Sigma_{\text{lf}}^{\text{inter}} = \frac{-1}{2A_0} \left(1 + \frac{(4I+1)}{6I} \frac{a}{A_0} [m - m'] \right) = \frac{-1}{2A_0}. \tag{27}$$

For the hf-manifold, the sign of Eq. (26) is the opposite so $\Sigma_{\text{hf}}^{\text{inter}} = -\Sigma_{\text{lf}}^{\text{inter}}$ and for the center-field line of ^{14}N, $\Sigma_{\text{cf}}^{\text{inter}} = 0$.

2.2.2 Intra-Manifold

For line m of any manifold, we have from Eq. (21)

$$\Sigma_{mlf}^{\text{intra}} = \frac{1}{(2I+1)a} \sum_{m' \neq m} \frac{\rho_{m'}}{(m'-m)}. \tag{28}$$

The average of $\Sigma_{mlf}^{\text{intra}}$ is zero, by symmetry and is difficult to compute for a general proton hyperfine pattern; however, for equivalent protons the sum may be calculated easily. For example, for $N = 12$, the results are given in column 2 of Tables 2 and 3. The other entries in Table 2 are sample calculations for the *lf*-manifold of Fig. 1 while Table 3 gives the results for the *hf*-manifold.

2.2.3 Dispersion Height

For line m of the lf-manifold, Eq. 20,

$$\frac{V_{\text{disp}mM}}{V_{\text{pp}mM}} = \frac{V_{\text{disp}mM}^{\text{inter}}}{V_{\text{pp}mM}^{\text{inter}}} + \frac{V_{\text{disp}mM}^{\text{intra}}}{V_{\text{pp}mM}^{\text{intra}}} = -\frac{8\sqrt{3}}{9} \frac{(2I+1)VC}{\gamma}$$

$$\left[\frac{-1}{2A_0} \left(1 + \frac{(4I+1)}{6I} \frac{a}{A_0} [m - m'] \right) + \frac{1}{(2I+1)a} \sum_{m' \neq m} \frac{\rho_{m'}}{(m'-m)} \right]. \tag{29}$$

Table 2 The intra-manifold sum in Eq. (28) and sample calculations for the HSE ^{15}N spectrum of Fig. 1 lf-manifold

If proton line m	$\sum_{m' \neq m} \frac{\rho_{m'}}{(m'-m)}$	$\delta H_{mM}^{\text{intra}}$, mG, Eq. (31)	B_m, G, Eq. (35)	$V_{\text{disp}mM}^{\text{inter}} / V_{\text{pp}mM}^{\text{inter}}$	$V_{\text{disp}mM}^{\text{intra}} / V_{\text{pp}mM}^{\text{intra}}$
0	− 0.186	0.0327	0.277	0.00748	0.0859
1	− 0.235	0.495	0.277	0.00764	0.108
2	− 0.301	3.49	0.275	0.00779	0.139
3	− 0.359	13.9	0.270	0.00794	0.166
4	− 0.352	30.6	0.260	0.00809	0.163
5	− 0.226	31.4	0.250	0.00825	0.104
6	0.00	0.00	0.246	0.00840	0.00
7	0.226	− 31.4	0.250	0.00855	− 0.104
8	0.352	− 30.6	0.260	0.00871	− 0.163
9	0.359	− 13.9	0.270	0.00886	− 0.166
10	0.301	− 3.49	0.275	0.00901	− 0.139
11	0.235	− 0.495	0.277	0.00916	− 0.108
12	0.186	− 0.0327	0.277	0.00932	− 0.0859
Average		0	0.266	0.0084	0

Parameters: $A_0 = 22$ G, $a = 0.4$ G, $K_{\text{ex}}C/\gamma = 0.24$ G, $\Delta H_{\text{pplf}}^L(0) = 0.45$ G, and $\Delta H_{\text{pphf}}^L(0) = 0.69$ G. Line shifts due to inter-manifold interactions, leading term of Eq. (31), are less than 0.1 mG

Table 3 The intra-manifold sum in Eq. (28) and sample calculations for the HSE ^{15}N spectrum of Fig. 1 hf-manifold

lf proton line m	$\sum_{m'\neq m}\frac{\rho_{m'}}{(m'-m)}$	$\delta H_{mM}^{\text{intra}}$, mG, Eq. (31)	B_m, G, Eq. (35)	$V_{\text{disp}mM}^{\text{inter}}/V_{\text{pp}mM}^{\text{inter}}$	$V_{\text{disp}mM}^{\text{intra}}/V_{\text{pp}mM}^{\text{intra}}$
0	0.186	0.0327	0.277	− 0.00932	0.0859
1	0.235	0.495	0.277	− 0.00916	0.108
2	0.301	3.49	0.275	− 0.00901	0.139
3	0.359	13.9	0.270	− 0.00886	0.166
4	0.352	30.6	0.260	− 0.00871	0.163
5	0.226	31.4	0.250	− 0.00855	0.104
6	0.00	0.00	0.246	− 0.00840	0.00
7	− 0.226	− 31.4	0.250	− 0.00825	− 0.104
8	− 0.352	− 30.6	0.260	− 0.00809	− 0.163
9	− 0.359	− 13.9	0.270	− 0.00794	− 0.166
10	− 0.301	− 3.49	0.275	− 0.00779	− 0.139
11	− 0.235	− 0.495	0.277	− 0.00764	− 0.108
12	− 0.186	− 0.0327	0.277	− 0.00748	− 0.0859
Average		0	0.266	− 0.0084	0

The same parameters as Table 2

Averaging over the lf-manifold $\Sigma_{m\text{lf}}^{\text{intra}} = 0$, so the average is only due to the inter-manifold interactions as follows:

$$\frac{V_{\text{displf}}}{V_{\text{pplf}}} = \frac{4}{3\sqrt{3}}\frac{(2I+1)VC}{\gamma A_0}. \tag{30}$$

For the hf-manifold, the sign of Eq. (30) is the opposite and for ^{14}N, the result is the same. Equation (30) is the same as the result as for $(2I+1)VC \gg \gamma a$ [18] as long as $(2I+1)VC \ll \gamma A_0$. Above this limit, entering into the nitrogen dark zone, $V_{\text{displf}}/V_{\text{pplf}}$ is no longer linear in VC; however, it is easily interpolated all the way up to spectrum narrowing using Tables 3 and 5 of Ref. [13] or the expressions in Ref. [5]. In this paper, these corrections are negligible except at 340 K; there, we make the appropriate corrections.

2.2.4 Line Shifts

From Eq. (19) the shift of line m in the low-field manifold is given by

$$\delta H_{m\text{lf}} = \delta H_{mM}^{\text{inter}} + \delta H_{mM}^{\text{intra}} = -\rho_{mM}\left(\frac{(2I+1)VC}{\gamma}\right)^2 [\Sigma_{m\text{lf}}^{\text{inter}} + \Sigma_{m\text{lf}}^{\text{intra}}]. \tag{31}$$

Averaging, $\Sigma_{m\text{lf}}^{\text{intra}}$ vanishes. The average of ρ_m is $1/(N+1)$, so the average value of $\rho_m K$, where K is a constant is $K/(N+1)$ and the average of $\rho_m m$ is given by $\sum \rho_m m/(N+1) = <m>/(N+1) = N/[2(N+1)]$.

Therefore, the average of Eq. (31), given by

$$\delta H_{m\text{lf}} = \frac{\rho_m}{2I+1}\left(\frac{(2I+1)VC}{\gamma}\right)^2 \frac{1}{2A_0}\left[\left(1+\frac{(4I+1)}{6I}\frac{a}{A_0}[m-m']\right)\right] \tag{32}$$

after a few steps, yields

$$H_{\text{lf}} - H(0)_{\text{lf}} = \frac{1}{N+1}\frac{1}{2I+1}\left(\frac{(2I+1)VC}{\gamma}\right)^2 \frac{1}{2A_0} \tag{33}$$

Comparing this result for the region $(2I+1)VC \ll \gamma a$ with that at $(2I+1)VC \gg \gamma a$, where

$$H_{\text{lf}} - H(0)_{\text{lf}} = \frac{1}{2I+1}\left(\frac{(2I+1)VC}{\gamma}\right)^2 \frac{1}{2A_0} \tag{34}$$

shows that the initial shift is a factor of $1/(N+1)$ smaller. The remarks following Eq. (30) are applicable to Eq. (34), where, upon entering into the nitrogen dark zone, the line shifts no longer vary as $(VC)^2$ but may be easily interpolated all the way up to spectrum narrowing using Refs. [5, 13].

2.2.5 Line Broadening

The broadening of line m in any manifold due to HSE is given by [7]

$$\Delta H_{\text{pp}mM}^{\text{L}} - \Delta H_{\text{pp}M}^{\text{L}}(0) = \frac{2}{\gamma\sqrt{3}}K_{\text{ex}}C\left(1-\frac{\rho_m}{2I+1}\right). \tag{35}$$

And the average

$$\Delta H_{\text{pp}M}^{\text{L}} - \Delta H_{\text{pp}M}^{\text{L}}(0) = \frac{2}{\gamma\sqrt{3}}K_{\text{ex}}C\left(1-\frac{1}{(2I+1)(N+1)}\right). \tag{36}$$

The term in the parentheses is 0.962 for ^{15}N and 0.974 for ^{14}N. The initial broadening for $(2I+1)VC \ll \gamma a$ is about 2 times that for $(2I+1)V \gg \gamma a$ for ^{15}N and 3/2 times for ^{14}N where the term in the parentheses becomes 1/2 or 2/3, respectively.

The broadening of line m due to DD is given by [14]

$$\Delta H_{\text{pp}mM}^{\text{L}} - \Delta H_{\text{pp}M}^{\text{L}}(0) = \frac{2}{\gamma\sqrt{3}}(W_{\text{dd}}^{\text{like}} + W_{\text{dd}}^{\text{unlike}})C, \tag{37}$$

where the superscripts denote like- and unlike-spins, respectively. From Eq. (6) of Ref. [14], in the HVL,

$$W_{\text{dd}}^{\text{like}} = \frac{\rho_m}{2I+1}\kappa^2\frac{3}{8}J^{(0)}N_{\text{A}}(10^{-3}) \tag{38}$$

$$W_{\text{dd}}^{\text{unlike}} = \left(1-\frac{\rho_m}{2I+1}\right)\kappa^2\frac{5}{24}J^{(0)}N_{\text{A}}(10^{-3}). \tag{39}$$

From Eq. 5, in the HVL limit,

$$W_{dd} = \kappa^2 \frac{10I + 9}{24(2I + 1)} J^{(0)} N_A (10^{-3}) \tag{40}$$

W_{dd} pertains to a spectrum without proton hfs; however, by assuming that it is approximately correct at large concentrations when the manifold has collapsed, Eq. (37) becomes

$$\Delta H^L_{ppmM} - \Delta H^L_{ppM}(0) = \frac{2}{\gamma\sqrt{3}} W_{dd} \frac{1}{10I + 9} [4\rho_m + 5(2I + 1)]C \tag{41}$$

and the average

$$\Delta H^L_{ppM} - \Delta H^L_{ppM}(0) = \frac{2}{\gamma\sqrt{3}} W_{dd} \frac{1}{10I + 9} \left[\frac{4}{N + 1} + 5(2I + 1)\right] C. \tag{42}$$

The total line width is given by the sum of Eqs. (35) and (41) and their averages by the sum of Eqs. (36) and (42).

2.2.6 Spectra in the Proton Perturbation Region $|V|C \ll \gamma a$

Figure 1 shows an instructive example spectrum of an ^{15}N spectrum with hyperfine coupling to 12 equivalent protons producing 13 lines of binomial relative intensities spaced by $a_p = 0.400$ G undergoing HSE with $V_{ex}C/\gamma = 0.120$ G or $K_{ex}C/\gamma = 0.240$ G. The line widths for $C \to 0$ are $\Delta H^L_{pplf}(0) = 0.450$ G and $\Delta H^L_{pphf}(0) = 0.690$ G. At $C = 0$, the lf-manifold is resolved at $\chi_{lf} = 3.2$ and the hf-manifold line unresolved at $\chi_{hf} = 2.09$. Figure 1 is constructed by placing 13 proton lines at positions shifted by δH_{mlf} from their positions given by Eq. (22) and listed in column 3 of Tables 2 and 3. These shifts are extremely small for the inter-manifold under these conditions, less than 0.1 mG. In (a), at each position, a Lorentzian absorption is placed with amplitude given by Eq. (17) and line width by Eq. (35) using the broadening given in column 4 of Tables 2 and 3. On this scale, only 9 lines are discernable. In (b), at each position, a Lorentzian dispersion due to intra-manifold exchanges of amplitude given by Eq. (29) given by the 6th column of Tables 2 and 3 and in (c) the dispersions due to inter-manifold exchanges using the fifth column. Part (b) is amplified by a factor of 3 and (c) by a factor of 30; thus, the intra-manifold dispersion lines are not small while those due to inter-manifold interaction are. The bold lines in (a)–(c) are the sums of the proton lines where the quantities $\Delta H^{man}_{pp\mp1/2}$, $V^{man}_{pp\mp1/2}$, and $Y^{man'}_{disp\mp1/2}$ are defined. Figure 1d shows the sum of all of the lines in (a)–(c). In (d), the quantities V^{man}_{maxM}, V^{man}_{minM}, and Ω^{man}_{ppM} are defined. Note that the peak-to-peak heights of the admixtures, $Y^{man'}_{maxM} - Y^{man'}_{minM}$, are larger than V^{man}_{ppM} because of the addition of the intra-manifold dispersion lines, 1(c). The sums of the lines in (b) are antisymmetric about the manifold centers and have the general appearance of absorption lines, as was observed in the 3-line case in Fig. 5c of Ref. [13]. It is imperceptible in Fig. 1 that the spectrum is asymmetric; however, the addition of the inter-manifold dispersions, 1c, renders it so. It is this asymmetry that is exploited by the 2-point method to separate HSE and DD. The ratio of the two heights, $Y^{man'}_{maxM}$ and $Y^{man'}_{minM}$, r_M, yields a quantitative measure of the asymmetry as follows:
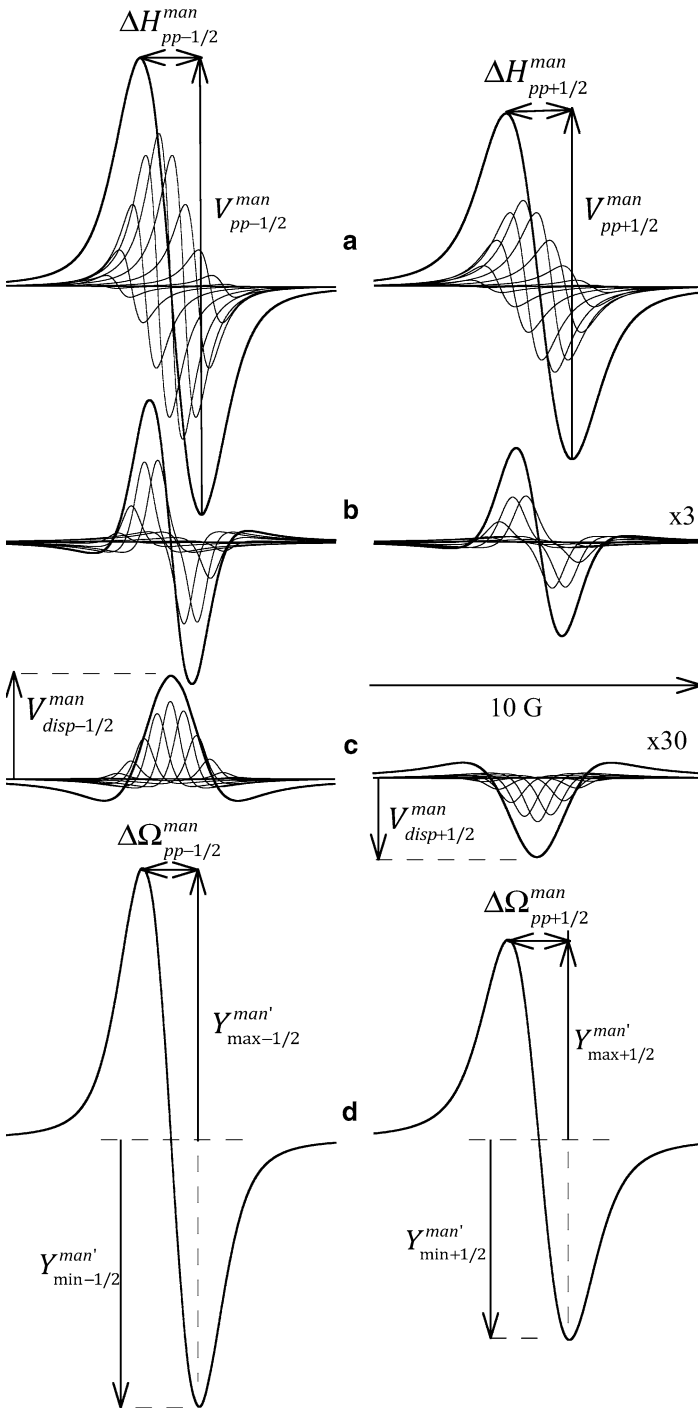
◄**Fig. 1** ^{15}N EPR spectrum with hyperfine coupling to 12 equivalent protons producing 13 lines of binomial relative intensities spaced by $a_p = 0.400$ G undergoing HSE with $V_{ex}C/\gamma = 0.120$ G or $K_{ex}C/\gamma = 0.240$ G. The line widths at $C = 0$ are $\Delta H^L_{pplf}(0) = 0.450$ G and $\Delta H^L_{pphf}(0) = 0.690$ G. On this scale, only nine lines are discernible. The first trace shows the absorptions and the second and third traces, the intra- and inter-manifold dispersions, respectively. Part **b** is amplified by a factor of 3 and **c** by a factor of 30. The bold lines in **a**–**c** are the sums of the proton lines where the quantities ΔH^{man}_{ppM}, V^{man}_{ppM}, and $Y^{man'}_{dispM}$ are defined. **d** Sum of all of the lines in **a**–**c** and defines the quantities V^{man}_{maxM}, V^{man}_{minM}, and Ω^{man}_{ppM}

$$r_M = \frac{Y^{man'}_{maxM}}{Y^{man'}_{minM}}. \tag{43}$$

The fitting method models 1(d) as admixtures of absorptions and inter-manifold dispersions and uses the relative heights of these two components to separate HSE and DD. To be successful, the presence of 1(b) must not lead to intolerable errors.

To gain a better appreciation of the various parameters in Fig. 1, Fig. 16 of "Appendix 1" shows an absorption–dispersion admixture with greatly exaggerated values of $V^{inter}_{dispmM}/V^{inter}_{ppmM}$. To put Fig. 1 into perspective, note that $K_{ex}C/\gamma = 0.24$ G corresponds to $C = 8$ mM for $K_{ex}/\gamma = 30$ G/M.

Using the perturbation results to compute the spectrum in Fig. 1 affords the tremendous advantage of being able to measure each of the parameters in Fig. 1 separately and relate them to those of Eqs. (21), (23), (29), and (36) which yield the rate constant K_{ex}.

Figure 1 illustrates the case for HSE. For DD, the figure is similar except that the dispersion components are of the opposite sign, so we do not display it. Call this spectrum the DD counterpart to Fig. 1. In fact, if we choose $V_{dd} = -0.12$ G, the line shifts are identical and the values of V_{dispmM}/V_{ppmM} are the same magnitude but opposite sign. A significant difference is in the line width variation, Eq. (41), as shown in Table 4. In the DD case, the peak-to-peak heights of the admixtures, $Y^{man'}_{maxM} - Y^{man'}_{minM}$, are smaller than V^{man}_{ppM}.

2.3 The Fitting Method

An experiment yields spectra like that in Fig. 1d, admixtures of absorption and dispersion components, and our task is to obtain the best estimate of K_{ex} together with a reliable estimate of the uncertainty. For the spectrum of the counterpart to Fig. 1, we obtain W_{dd}, and in the general case K_{ex} and W_{dd} separately. We apply the approach that has been successful over the years beginning with the four-point method [20] and evolving into least-squares fitting method [22], using the Voigt line shape to approximate the experimental spectrum. For $C \to 0$, only the absorption component is needed in principle; however, in practice instrument dispersion arises due to slightly unbalanced microwave bridges. Fitting allows the removal of the dispersion artifact.

We may apply the Voigt to absorptions such as that in Fig. 1a, to dispersions such as that in Fig. 1c, and thus to admixtures such as that in Fig. 1d is the basis of the method. It is a phenomenological approach.

Therefore, we fit simulated spectra such as that in Fig. 1d and experimental spectra to the following:

Table 4 Sample calculations for the lf-manifold of the DD counterpart to Fig. 1 ^{15}N spectrum not shown

lf proton line m	$\sum\limits_{m'\neq m} \frac{\rho_{m'}}{(m'-m)}$	$\delta H_{mM}^{\text{intra}}$, mG, Eq. (31)	B_m, G, Eq. (35)	$V_{\text{disp}mM}^{\text{inter}}/V_{\text{pp}mM}^{\text{inter}}$	$V_{\text{disp}mM}^{\text{intra}}/V_{\text{pp}mM}^{\text{intra}}$
0	-0.186	0.0327	0.346	-0.00748	-0.0859
1	-0.235	0.495	0.347	-0.00764	-0.108
2	-0.301	3.49	0.349	-0.00779	-0.139
3	-0.359	13.9	0.354	-0.00794	-0.166
4	-0.352	30.6	0.363	-0.00809	-0.163
5	-0.226	31.4	0.373	-0.00825	-0.104
6	0.00	0.00	0.378	-0.00840	0.00
7	0.226	-31.4	0.373	-0.00855	0.104
8	0.352	-30.6	0.363	-0.00871	0.163
9	0.359	-13.9	0.354	-0.00886	0.166
10	0.301	-3.49	0.349	-0.00901	0.139
11	0.235	-0.495	0.347	-0.00916	0.108
12	0.186	-0.0327	0.346	-0.00932	0.0859
Average		0	0.357	-0.00840	0

Parameters: $^{15}A_0 = 22$ G, $a = 0.4$ G, $V_{dd}C/\gamma = -0.12$ G, $\Delta H_{\text{pp}-1/2}^{\text{L}}(0) = 0.45$ G,   and $\Delta H_{\text{pp}+1/2}^{\text{L}}(0) = 0.69$ G. Line shifts due to inter-manifold interactions are less than 0.1 mG for all lines

$$Y' = \sum_M [V_{\text{pp}M}^{\text{man}} S_M'^{\text{abs}} + V_{\text{disp}M}^{\text{man}} S_M'^{\text{disp}}], \tag{44}$$

where $S_M'^{\text{abs}}$ is the sum-function approximation to the Voigt absorption of unit peak-to-peak intensity as follows:

$$S_M'^{\text{abs}} = -\left\{ \eta_{\text{abs}M} \frac{-8\xi_M}{(3+\xi_M^2)^2} + (1-\eta_{\text{abs}M})\frac{\sqrt{e}}{2}e^{\frac{-\xi_M^2}{2}} \right\}, \tag{45}$$

where $-8\xi_M(3+\xi_M^2)^2$ and $\frac{\sqrt{e}}{2}e^{\frac{-\xi_M^2}{2}}$ are the Lorentzian and Gaussian absorptions of unit peak-to-peak height, respectively.

$S_M'^{\text{disp}}$ is the sum-function approximation to the Voigt dispersion of unit extremum intensity as follows [23]:

$$S_M'^{\text{disp}} = \left\{ \eta_{\text{disp}M} \frac{3(3-\xi_M^2)}{(3+\xi_M^2)^2} + (1-\eta_{\text{disp}M})(1-\xi_M^2-0.27\xi_M^4)e^{\frac{-\xi_M^2}{2}} \right\}. \tag{46}$$

Unfortunately, Eq. (16) of Ref. [23] has a typographical error omitting the $-\xi_M^4$ term.

In Eqs. (45) and (46)

$$\xi_M = 2\frac{H-H_M}{\Delta H_{\text{pp}M}^{\text{man}}}, \tag{47}$$

where H is the swept magnetic field, and H_M and $\Delta H_{\text{pp}M}^{\text{man}}$ are the resonance field and peak-to-peak line width of the manifold, respectively. The one-to-one relationship (map) of the mixing parameter $\eta_{\text{abs}M}$ with the Voigt parameter χ_M may be found by

fitting Eq. (44) to either a Voigt or any pattern. In principle, χ_M may also be obtained from $\eta_{\mathrm{disp}M}$; however, the accuracy is considerable poorer. It was important to develop Eq. (46) with a variable $\eta_{\mathrm{disp}M}$ to ensure a good fit with the IMB dispersion component so as not to distort the other parameters in the fit.

From a fit value of $\eta_{\mathrm{abs}M}$, a value of χ_M is computed and $\Delta H_{\mathrm{pp}M}^{\mathrm{L(Voigt)}}$ is obtained from the Dobrayakov–Lebedev relation [24]

$$\Delta H_{\mathrm{pp}M}^{\mathrm{L(Voigt)}} = \Delta H_{\mathrm{pp}M}^{\mathrm{man}} \frac{\left(-1 + \sqrt{1 + 4\chi_M^2}\right)}{2\chi_M^2}. \tag{48}$$

Equation (8) then yields $\Delta H_{\mathrm{pp}M}^{\mathrm{G(Voigt)}}$. The fit of Eq. (44) to a manifold due to 12 equivalent protons, with a dispersion admixture of $V_{\mathrm{disp}M}/V_{\mathrm{pp}M} = 0.3$ shows a residual with a maximum of 0.5% (Fig. 9a of [23]), $\Delta H_{\mathrm{pp}M}^{\mathrm{L(Voigt)}}$ are accurate to 1.1% at $\chi_M = 2.5$ (incipiently resolved) and less than 1% for $\chi_M < 2.3$. See Table 5 of Ref. [23]. Therefore, the fidelity of Eq. (44) has been established with IHB admixtures for $C \to 0$. To apply it to spectra undergoing HSE and/or DD, we require that as $|V|C$ increases, the line shape is still accurately given by the Voigt. This assumption is easily checked by fitting simulations of Eq. (1) and we show in "Appendix 2" that they are indeed excellent Voigts for both HSE and DD.

To evaluate $\langle V_{\mathrm{disp}M}/V_{\mathrm{pp}M} \rangle$ from measured values of $V_{\mathrm{disp}M}^{\mathrm{man}}/V_{\mathrm{pp}M}^{\mathrm{man}}$ it is necessary to take into account that as χ_M increases, $V_{\mathrm{disp}M}^{\mathrm{man}}$ decreases more rapidly than $V_{\mathrm{pp}M}^{\mathrm{man}}$ [23]. This problem was treated in detail in Ref. [23] for $C \to 0$. The discrepancies of values of $\langle V_{\mathrm{disp}M}^{\mathrm{man}}/V_{\mathrm{pp}M}^{\mathrm{man}} \rangle$ directly measured from the separate components, or from admixtures fitted to Eq. (45) are negligible, $< 0.3\%$. The desired transformation from $V_{\mathrm{disp}M}^{\mathrm{man}}/V_{\mathrm{pp}M}^{\mathrm{man}}$ to $V_{\mathrm{disp}M}/V_{\mathrm{pp}M}$ may be effected by interpolation of the results are given in column 6 of Table 5 of Ref. [23], or, to within 1% by the following:

$$\left\langle \frac{V_{\mathrm{disp}M}}{V_{\mathrm{pp}M}} \right\rangle = \theta(\chi_M) \frac{V_{\mathrm{disp}M}^{\mathrm{man}}}{V_{\mathrm{pp}M}^{\mathrm{man}}}, \tag{49}$$

where

$$\theta(\chi_M) = 1 + 0.1\chi_M - 0.019\chi_M^2. \tag{50}$$

To proceed, we make two assumptions:

2.3.1 Assumption 1

$\Delta H_{\mathrm{pp}M}^{\mathrm{L(Voigt)}}$ is equal to the average value of the Lorentzian line widths in the manifold:

$$\Delta H_{\mathrm{pp}M}^{\mathrm{L(Voigt)}} = \langle \Delta H_{\mathrm{pp}M}^{\mathrm{L}} \rangle. \tag{51}$$

We have used this assumption in the past [11, 18, 19, 25–28] on simulated and experimental spectra and have obtained reasonable results. Here, we confirm this assumption for $(2I + 1)|V|C \ll \gamma a$ by fitting Eq. (44) to Fig. 1d and add a high level of confidence by comparing $\Delta H_{\mathrm{pp}M}^{\mathrm{L(Voigt)}}$ for the experimental results for deuterated vs. protonated Tempol.

2.3.2 Assumption 2

The Voigt fit value of $\langle V_{\text{disp}M}^{\text{man}}/V_{\text{pp}M}^{\text{man}}\rangle$ transformed by Eq. (49) is equal to the average of $\langle V_{\text{disp}M}/V_{\text{pp}M}\rangle$.

This assumption has not been tested in the past because all of the experiments were extended to values of C well beyond the proton intermediate regime and fits to the data were dominated by the (much) larger values of $V_{\text{disp}M}^{\text{man}}/V_{\text{disp}M}^{\text{man}}$ where the lines were Lorentzian anyway. We shall see that this assumption results in significant errors for the proton dark zone because of the interference of the intra-manifold dispersion components.

It is important to note the difference in the resonance fields, shown in Fig. 1, or better, from "Appendix 1", and the point at which the spectrum crosses the baseline. The former is available from a fit of the spectrum, but not from the spectrum itself. Equations (44) and (58) include explicitly the overlap between the nitrogen manifolds. In principle, $\Delta H_{\text{pp}M}^{\text{man}}$ is different from $\Delta \Omega_{\text{pp}M}^{\text{man}}$, but they are the same within experiment error in this work. Therefore, $\Delta H_{\text{pp}M}^{\text{man}}$ can be determined by fitting or by direct measurement; the advantage of the former is that it's less noisy and is determined to higher precision.

From values of $\langle H_M\rangle$, the line shifts of the manifolds due HSE and/or DD may be computed. For cases in which HSE dominates, these shifts may be used to estimate the mean time that two nitroxides reside within a cage as detailed in Refs. [6, 25, 26, 29–31]; however, this is outside the scope of the present paper.

From quantities derived from fitting a spectrum to Eq. (44) or (55), the concentration broadening, B_M, is computed from the follow:

$$B_M = \Delta H_{\text{pp}M}^{\text{L(Voigt)}} - \Delta H_{\text{pp}}^{\text{L}}(0), \tag{52}$$

which, when plotted against C, give straight lines of slope, $B_M^{'}$, and intercept $\Delta H_{\text{pp}}^{\text{L}}(0)$.

$$B_M^{'} = \text{d}\Delta H_{\text{pp}M}^{\text{L(Voigt)}}/\text{d}C \tag{53}$$

In the case of HSE for ^{14}N, B_M is larger for lf and hf than for cf upon entering into the nitrogen dark zone; however, the average over the three lines is linear with C all of the way through coalescence and narrowing of the nitrogen manifolds [13]. In this study, the effect is barely outside of experimental error. Therefore, in this work, $B_M^{'}$ is independent of M allowing us to find mean values and estimates of the errors from the standard deviations.

Plots of $\langle V_{\text{disp}M}/V_{\text{pp}M}\rangle$ against B_M/A_0 are linear, as follows:

$$\langle\frac{V_{\text{disp}M}}{V_{\text{pp}M}}\rangle = k_M \frac{B_M}{A_0}. \tag{54}$$

Giving two or three values of k_M for ^{15}N and ^{14}N, respectively.

From $B^{'}$ and k, the rate constants are found from Ref. [18] as follows:

$$K_{\text{ex}} = \left(\frac{\sqrt{3}\gamma}{2}\right)2\left(\frac{21k+8}{36}\right){}^{15}B^{'}, \tag{55}$$

$$K_{\text{ex}} = \left(\frac{\sqrt{3}\gamma}{2}\right)\frac{3}{2}\left(\frac{19k + 8}{27}\right){}^{14}B', \tag{56}$$

$${}^{15}W_{\text{dd}} = \left(\frac{\sqrt{3}\gamma}{2}\right)\left(\frac{28 - 21k}{36}\right){}^{15}B', \tag{57}$$

$${}^{14}W_{\text{dd}} = \left(\frac{\sqrt{3}\gamma}{2}\right)\left(\frac{19 - 19k}{27}\right){}^{14}B'. \tag{58}$$

To compare the DD results of the two isotopes,

$${}^{14}W_{\text{dd}} = \frac{19}{21}\,{}^{15}W_{\text{dd}} \tag{59}$$

where the superscript is the atomic number of the isotope.

2.4 Theory of the Two-Point Method

The algorithm introduced in Ref. [14] and extended to IHB spectra in Ref. [17] requires the measurement of two points, at the maximum and minimum of each manifold, as illustrated in Fig. 1. The asymmetry parameter, p_M, for manifold M is defined in Eq. (15) of Ref. [17] as follows:

$$p_M = \frac{\sqrt{3}}{2}\left(1 - \sqrt{2|r_M| - 1}\right) \tag{60}$$

From the equation following Eq. (17) and Eq. (28) of Ref. [14], the rates of transfer of spin coherence for lf, are as follows:

$$VC = -\frac{1}{2I + 1}p_{\text{lf}}\,{}^{15}A_0, \tag{61}$$

with the opposite sign for hf. Therefore, with a measurement of A_0, the slopes of linear plots of the right-hand side of Eq. (61) versus C yield the rate constants of spin coherence transfer, V.

For Lorentzian lines,

$$p_{mM} = -\frac{3\sqrt{3}}{4}\frac{V_{\text{disp}mM}}{V_{\text{pp}mM}}. \tag{62}$$

To pass from p_{mM} to p_M^{man}, the value measured from an IHB spectrum, we invoke assumption 2 above, which has been justified in the Appendix to Ref. [17]

$$p_M = -\frac{3\sqrt{3}}{4}\langle V_{\text{disp}M}/V_{\text{pp}M}\rangle. \tag{63}$$

Thus, both p_M and $V_{\text{disp}M}/V_{\text{pp}M}$ contain the same information, the former obtained from two points on each manifold and the latter from a fit to all of the points including manifold overlap.

2.5 Notation

We note that the notations in [14,17] are different, being related by the following:

$$V_{dd} = -\frac{K_{dsct}}{2I + 1},$$ (64)

$$W_{dd} = K_{dsd} + \frac{K_{dsct}}{2I + 1}.$$ (65)

3 Materials and Methods

14NH was prepared from triacetonamine. 15 NH, and 15 ND (purity 95%) were prepared from isotope-enriched triacetonamine-^{15}N and ^{15}N-d$_{17}$, respectively, from literature procedures [32]. Triacetonamine-^{15}N was prepared from [15]NH$_4$Cl (isotope enrichment 99.9%) according to the method by Pirrwitz and Schwarz [33] with minor modifications (Scheme 2) [34]. An additional source of 14NH, which we denote 14 NHΣ, was purchased from Sigma and used as received. 60 wt% aqueous glycerol (98%) was prepared using distilled water. Nitroxide solutions were prepared gravimetrically from stock solutions with concentrations varying from 0.1 to 40–50 mM for 15 NH, 15 ND, and 14 NHΣ and 0.1–88 mM for 14 NH. Samples were drawn into 50-μL disposable pipettes and sealed at both ends with a flame. EPR spectra were obtained of each of the four series of samples at X-band at 273, 298, 323, 333, and 340 K with a Bruker EMX Plus spectrometer equipped with a nitrogen-flow temperature controller with a precision of 0.1 K. The following parameters were used throughout: microwave power, 0.2 mW; modulation amplitude, 0.1 G; modulation frequency, 100 kHz; time constant, 5.12 ms; conversion time, 40 ms. The field-sweeps and resolutions, in parentheses, were as follows: 15 NH (50 G, 50 mG) 15 ND (50 G, 50 mG), 14 NH (75 G, 10 mG) and 14 NHΣ (75 G, 50 mG). Two or three spectra were recorded of each sample at each temperature, one after the other. A saturation curve, signal intensity vs. the square root of the microwave power, of 50-mM 14NH in 60 wt% glycerol at RT departed from linearity by 1.5% at 3 mW and 6% at 5 mW. For a 0.6-mM sample, the curve departed from linearity at 1.2 mM. Therefore, the measuring microwave power, 0.2 mW, is well below where any saturating effects may be observed.

3.1 Correcting for Instrumental Dispersion

Correcting for instrumental dispersion has been discussed in previous papers; see, for example, the Supplemental Information of Ref. [18] and references therein. Briefly, we exploit the fact that instrumental dispersion has the same sign for all values of M and correct by subtracting the dispersion for the central manifold from the other two for ^{14}N and subtracting the average value of the outer manifolds from the value of each manifold for [15]N. From ^{14}N, we obtain two values of $\langle p_M \rangle$ or $V_{dispM}^{man}/V_{dispM}^{man}$ from which an estimate of the systematic error may be obtained. From ^{15}N, only one value of each is available: we use the systematic error from ^{14}N as an

estimate for ^{15}N. Because we employ the slopes of the two measures of dispersion, an alternative method is available by finding the slope of the two outer lines for both isotopes yielding two values p_M or $V_{\mathrm{disp}M}^{\mathrm{man}}/V_{\mathrm{disp}M}^{\mathrm{man}}$ for either isotope. This latter alternative supposes that the instrumental dispersion is constant in a series of measurements at different values of C, a supposition that is rather good [18]. The two approaches give the same results within experimental error.

4 Results

4.1 Results from Perturbation Theory

The results of fitting the perturbation theory spectrum of Fig. 1d with Eq. (44) and applying the two-point method are given in columns 3 and 4 of Table 5. Results for the two-point method were obtained by measuring r_M, Eq. (43) on the spectrum of Fig. 1. The first entry in columns 3 and 4 pertain to the spectrum in Fig. 1d. The second entries give the results in which the intra-manifold were absent. In other words, comparing the first and second entries shows the effect of the intra-manifold dispersions on the final results. Table 5 shows that the values of $V_{\mathrm{disp}M}^{\mathrm{man}}/V_{\mathrm{pp}M}^{\mathrm{man}}$ are reduced by about 13% by the presence of the intra-manifold dispersions with the fit method, while the two-point method is only reduced by about 7%. However, the fit method is more accurate than the two-point method with or without the intra-manifold dispersions (Table 5).

Table 5 Comparison of perturbation and exact theories for ^{15}N $K_{\mathrm{ex}}C/\gamma = 0.24$ G

Method	Parameter	Perturbation lf	Perturbation hf	Equation (1) lf	Equation (1) hf
Two-point	p_M	− 0.0083[a]	0.0089[a]	− 0.0078	0.0087
		− 0.0078[b]	0.0086[b]	–	–
Two-point	$V_{\mathrm{disp}M}^{\mathrm{man}}/V_{\mathrm{pp}M}^{\mathrm{man}}$	0.0064[a]	− 0.0069[a]	− 0.0060	0.0060
		0.0060[b]	− 0.0066[b]	–	–
Fit	$V_{\mathrm{disp}M}^{\mathrm{man}}/V_{\mathrm{pp}M}^{\mathrm{man}}$	0.0074[a]	− 0.0076[a]	0.0056	− 0.0061
		0.0086[b]	− 0.0086[b]	–	–
Fit	$\Delta H_{\mathrm{pp}M}^{\mathrm{L(Voigt)}}$, G	0.727[a]	0.940[a]	0.704	0.927
		0.781[b]	1.01[b]	–	–
Fit	$\Delta H_{\mathrm{pp}M}^{\mathrm{G(Voigt)}}$, G	1.22[a]	1.25[a]	1.23	1.25
		1.32[b]	1.33[b]	–	–
Fit	$\Delta H_{\mathrm{pp}M}^{\mathrm{0(Voigt)}}$, G	1.64[a]	1.81[a]	1.63	1.80
		1.77[b]	1.93[b]	–	–
Measured[c]	$V_{\mathrm{pp}M}^{\mathrm{withintra}}/V_{\mathrm{pp}M}^{\mathrm{without}}$	1.19	1.16	–	–

Hyperfine coupling to 12 equivalent protons, $a_p = 0.400$ G. Input values: $\Delta H_{\mathrm{pplf}}^{\mathrm{L}}(0) = 0.450$ G, $\Delta H_{\mathrm{pphf}}^{\mathrm{L}}(0) = 0.690$ G, and $\langle V_{\mathrm{disp}M}^{\mathrm{inter}}/V_{\mathrm{disp}M}^{\mathrm{inter}}\rangle = 0.0084$. For $C = 0$, $\Delta H_{\mathrm{pphf}}^{\mathrm{G(Voigt)}} = 1.44$ G

[a]Including intra-manifold dispersions

[b]Excluding intra-manifold dispersions

[c]Taken directly from the spectrum

The final two columns of Table 5 are computed from the exact theory, Eq. (1), with the same input parameters as the perturbation spectrum in Fig. 1. The spectrum is displayed in Fig. 2.

Because the two manifolds are of different line shapes, we may compare them. The largest discrepancy between the two manifolds is for $V_{\mathrm{disp}M}^{\mathrm{man}}/V_{\mathrm{pp}M}^{\mathrm{man}}$: from fitting, 3% for Fig. 1 and 7% for Eq. (1); from two-point, 7% for Fig. 1 and 11% for Eq. (1).

Summarizing the discrepancies between perturbation theory and Eq. (1) for the lf-manifold: from fitting, $V_{\mathrm{disp}lf}^{\mathrm{man}}/V_{\mathrm{pplf}}^{\mathrm{man}}$, 14% and $\Delta H_{\mathrm{pplf}}^{\mathrm{L(Voigt)}}$, 0.6%; from two-point method, $V_{\mathrm{displf}}^{\mathrm{man}}/V_{\mathrm{pplf}}^{\mathrm{man}}$, 7%. The small discrepancy in $\Delta H_{\mathrm{pplf}}^{\mathrm{L(Voigt)}}$ shows that the Voigt shape extracts this value rather precisely.

The errors computed from the known input values, are as follows: from fitting $V_{\mathrm{displf}}^{\mathrm{man}}/V_{\mathrm{pplf}}^{\mathrm{man}}$, 33% and $\Delta H_{\mathrm{pplf}}^{\mathrm{L(Voigt)}}$, 1.5%; from two-point method $V_{\mathrm{displf}}^{\mathrm{man}}/V_{\mathrm{pplf}}^{\mathrm{man}}$, 29%.

We may determine the effect of the intra-manifold dispersions in Fig. 1 by omitting them and fitting or applying the two-point method. We find that the errors computed from the known input values are as follows: from fitting $V_{\mathrm{displf}}^{\mathrm{man}}/V_{\mathrm{ppl}M}^{\mathrm{man}}$, 2% and $\Delta H_{\mathrm{pplf}}^{\mathrm{L(Voigt)}}$, 9%; from two-point $V_{\mathrm{displf}}^{\mathrm{man}}/V_{\mathrm{pplf}}^{\mathrm{man}}$, 29%.

To summarize, errors in $V_{\mathrm{disp}M}^{\mathrm{man}}/V_{\mathrm{ppl}M}^{\mathrm{man}}$ are substantial using either method, those from the fitting method mostly provoked by the presence of the intra-manifold dispersions. The values of $\Delta H_{\mathrm{pp}M}^{\mathrm{L(Voigt)}}$, only available from the fitting method, are too large by 2% for lf and too small by 2% for hf. These errors are found both from the perturbation result, Fig. 1 and from Eq. (1). In other words, the Lorentzian line width is found with excellent precision from either Fig. 1 or Eq. (1). Note that $dB/dC = 0.267$ G/M for the manifolds at $K_{\mathrm{ex}}C/a\gamma = 0.600$, Eq. (36), is about twice that at $K_{\mathrm{ex}}C/a\gamma \gg 1$ where $dB/dC = 0.139$ G/M. See Eq. (36) and the comments immediately after.

4.2 Results from the Exact Theory, Eq. (1)

Spectra were computed from Eq. (1) for a ^{15}N nitroxide, $A_0 = 22$ G with hyperfine coupling to 12 equivalent protons, $a = 0.4$ G, as functions of $K_{\mathrm{ex}}C/\gamma$ or $W_{\mathrm{dd}}C/\gamma$ with $\Delta H_{\mathrm{pplf}}^{\mathrm{L}}(0) = 0.45$ G and $\Delta H_{\mathrm{pplf}}^{\mathrm{L}}(0) = 0.69$ G. The lf-manifolds of spectra simulated near the incipient resolution limit for HSE and DD are shown in Fig. 19 of "Appendix 2". The spectra were fit with Eq. (44) and treated with the two-point method.

Figure 2a shows the exact spectrum using the same parameters as Fig. 1; i.e., for $K_{\mathrm{ex}}C/\gamma = 0.24$ G. Figure 2b, c display the inter-manifold dispersions and the absorptions, respectively, derived from fits to Eq. (44). Because the model of Eq. (44) does not include an extra term for the intra-manifold dispersions, these cannot appear. It would be futile to attempt to include such an extra term in the fit function, because it has the same symmetry as the absorption and the fit parameters would be unstable to say the least. In finding a fit, Eq. (44) does very well in discriminating against the intra-manifold dispersions as evidenced by the small residuals overlaying the spectrum in Fig. 2a; however, the parameters for $V_{\mathrm{pp}M}^{\mathrm{man}}$ and
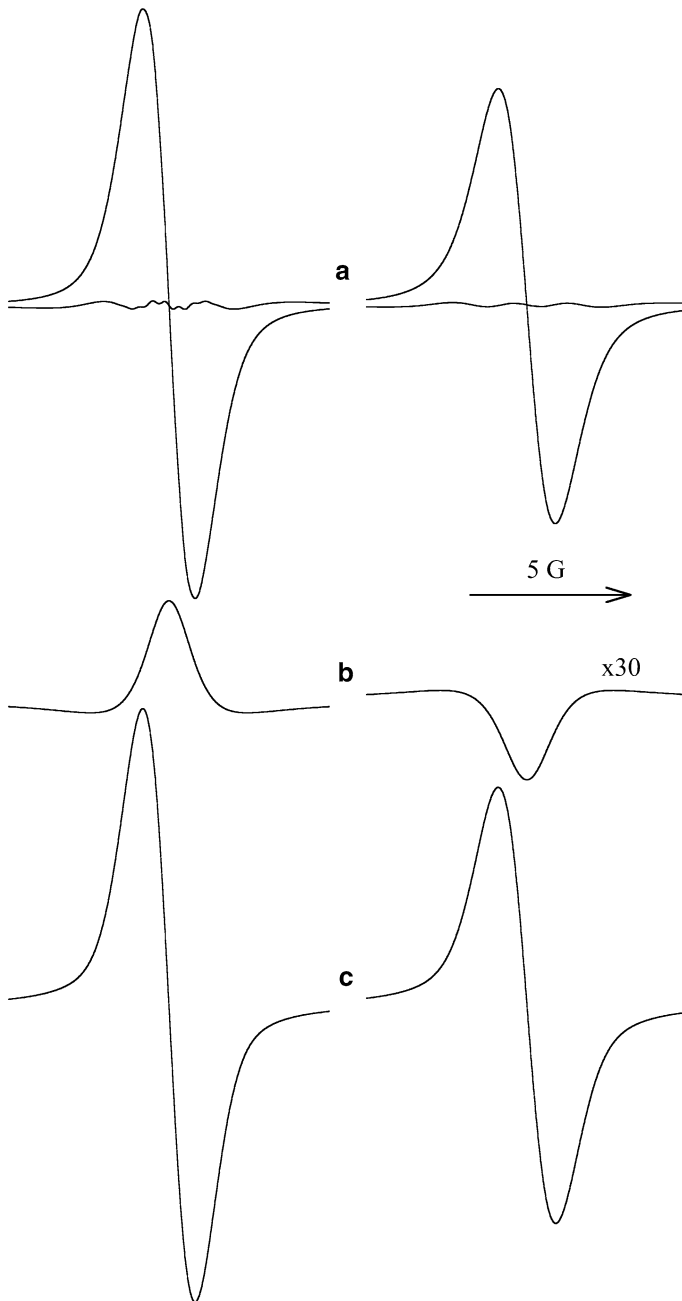
Fig. 2 a The exact spectrum computed with Eq. (1) of a ^{15}N nitroxide with the same parameters as Fig. 1. The spectrum fit to Eq. (44) produces the dispersion (**b**), and absorption (**c**) manifolds, respectively, and the residuals overlay the spectrum. The dispersion manifolds are amplified by 30

ΔH_{ppM}^{man} are in error. The magnitude of the errors may be judged by the perturbation results of Fig. 1 where all of the components are available separately. Table 5 shows the results of the fit and then those of the fit leaving out the intra-manifold dispersions.

Figure 3 shows the variation of line widths with $K_{ex}C/\gamma$, ΔH_{pphf}^{man}, squares; $\Delta H_{pphf}^{L(Voigt)}$, circles; and $\Delta H_{ppM}^{G(Voigt)}$, triangles. The straight line near the origin is the predicted initial values of $\Delta H_{pphf}^{L(Voigt)}$, Eq. (36). The inset shows more detail near the origin demonstrating that the initial increase in $\Delta H_{pphf}^{L(Voigt)}$ is accurately obtained under assumption 1. Calculating $d\left[\Delta H_{pphf}^{L(Voigt)}\right]/d[K_{ex}C/\gamma]$ numerically, not shown, we find that the slope from the fit extrapolated to the origin is 1.14 compared with the perturbation value of 1.11. Assumption 1 is extremely accurate in the most difficult portion of the data.

Figure 4 shows similar line-width data as Fig. 3 with the same input parameters except for DD. Note that while the initial slope of $\Delta H_{pphf}^{L(Voigt)}$ is larger than at higher values of C for HSE, Fig. 3 it is smaller for DD. The initial slope of $\Delta H_{pphf}^{L(Voigt)}$ is
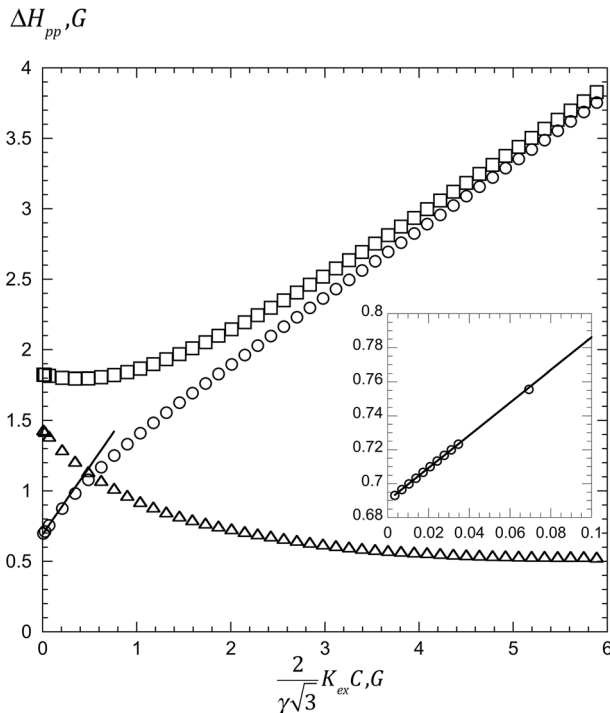
Fig. 3 Line widths for the hf manifold obtained from fitting spectra simulated from Eq. (1) for HSE: ^{15}N, $A_0 = 22$ G with hyperfine coupling to 12 equivalent protons, $a = 0.4$ G. Squares, ΔH_{pphf}^{man}; circles, $\Delta H_{pphf}^{L(Voigt)}$; and triangles, $\Delta H_{pphf}^{G(Voigt)}$. The straight line near the origin is the predicted initial values of $\Delta H_{pphf}^{L(Voigt)}$, Eq. (36). The inset shows more detail near the origin demonstrating that the initial increase in $\Delta H_{pphf}^{L(Voigt)}$ is accurately obtained under assumption 1
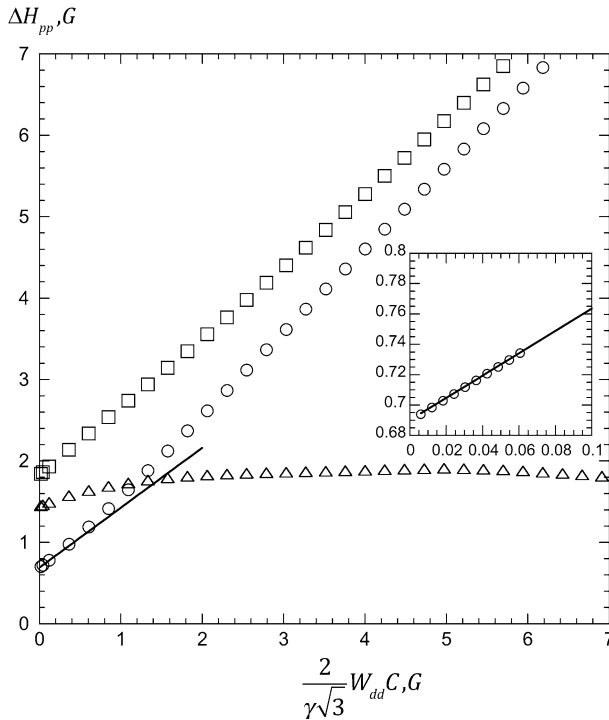
Fig. 4 The same as Fig. 3 except for DD. Note that the initial slope of $\Delta H_{\text{pphf}}^{\text{L(Voigt)}}$ is larger than at higher values of C for HSE, Fig. 3 but is smaller for DD. The initial slope of $\Delta H_{\text{pphf}}^{\text{L(Voigt)}}$ is computed from Eq. (42). Also note the interesting difference in the behavior of $\Delta H_{\text{pphf}}^{\text{G(Voigt)}}$, rapidly decreasing for HSE and slowly increasing before leveling out for DD

computed from Eq. (42). Also note the interesting difference in the behavior of $\Delta H_{\text{pphf}}^{\text{G(Voigt)}}$ in Figs. 3 and 4, rapidly decreasing for HSE and slowly increasing before leveling out for DD.

Figure 5 shows values of $V_{\text{disphf}}^{\text{man}}/V_{\text{pphf}}^{\text{man}}$ for the hf-manifold of the same spectra as Figs. 3 and 4 from fitting, circles and diamonds, and the two-point method, triangles and squares. For HSE, both methods yield reasonable results until line overlap near $VC/\gamma = 2$ degrades the fidelity of the two-point method. For DD, fitting yields reasonable results over the whole range while the two-point method is not useful over any range. The agreement, however, is deceptive on the scale of Fig. 5 through the proton dark zone. See the inset to Fig. 5. In an experiment, one usually finds a linear fit of $V_{\text{disphf}}^{\text{man}}/V_{\text{pphf}}^{\text{man}}$ as a function of C or B/A_0 (which is proportional to C) so errors in the value of $V_{\text{disphf}}^{\text{man}}/V_{\text{pphf}}^{\text{man}}$ and the slope are important. Figure 6 shows these errors as a function of $|V|C/\gamma a$. Unfortunately, both types of errors are large for both methods through the dark zone. Curiously, the two-point method is more accurate up to about $|V|C/\gamma a = 3$ because the underestimate of $V_{\text{disphf}}^{\text{man}}/V_{\text{pphf}}^{\text{man}}$, inherent in both methods, is offset by the overestimate due to line overlap. Above $|V|C/\gamma a = 5$, the two-point method yields less accurate results.
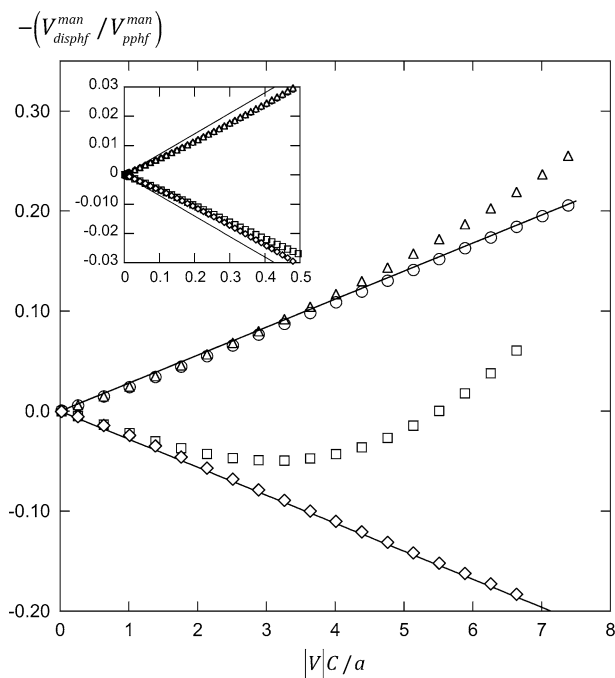
Fig. 5 Values of $-V_{\text{disphf}}^{\text{man}}/V_{\text{pphf}}^{\text{man}}$ from fitting, circles (HSE) and diamonds (DD) and from the two-point method, triangles (HSE) and squares (DD). Same parameters as in Fig. 3. The straight lines are the theoretical prediction computed with Eq. (30). Near the origin the two methods give similar results; however, overlap with the lf-manifold begins to yield erroneous results for the two-point method at higher concentrations

Doubly integrated intensities of experimental spectra are problematic because of limited sweep width and baseline drift; however, if a manifold is a good Voigt, they are easily calculated to excellent precision from ΔH_{ppM}^0 and $V_{\text{ppM}}^{\text{man}}$ by measuring χ_M and using Eqs. (18) and (34) of Ref. [20]. This procedure works for $C \rightarrow 0$ spectra because there is no underlying intra-manifold dispersion component that distorts the values ΔH_{ppM}^0 and $V_{\text{ppM}}^{\text{man}}$ from those pertaining strictly to the absorption component (Fig. 1a). The extent of this effect for the perturbation theory spectrum of Fig. 1 may be ascertained by comparing the results from spectra simulated with and without the intra-manifold dispersion components. The effect of the intra-manifold dispersions may be noted in Fig. 7, which is a plot of the doubly integrated intensities for spectra computed with Eq. (1) using the parameters given in the footnote to Table 5. The true doubly integrated intensity is constant because the intra-manifold dispersion integrates to zero. The true doubly integrated intensity would be difficult (almost impossible) to measure from an experimental spectrum because we measure over a finite magnetic field sweep width. Fortunately, because the values of ΔH_{ppM}^0 are too large and $V_{\text{ppM}}^{\text{man}}$ too small, the resulting apparent doubly integrated intensities are only 3% too large for HSE and 5% too small for DD.
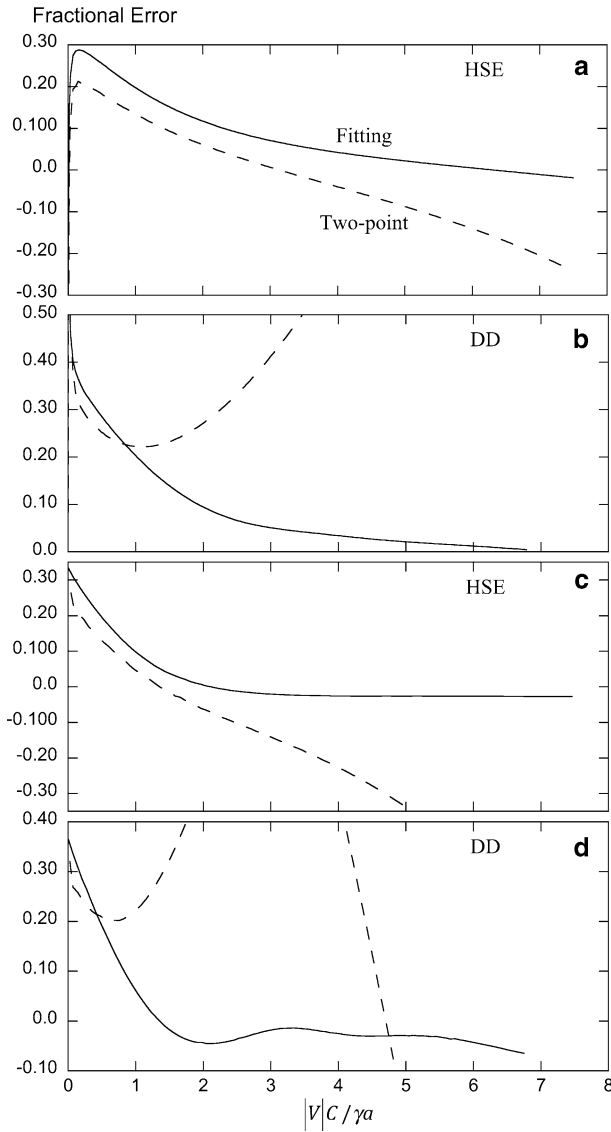
Fractional Error

Fig. 6 The fractional error in $\langle V_{\text{disphf}}/V_{\text{pphf}} \rangle$ by analyzing exact spectra computed from Eq. (1) for HSE (**a**) and DD (**b**). Fitting, solid lines and the two-point method, dashed lines. The fractional error in $\text{d}\langle V_{\text{disphf}}/V_{\text{pphf}}/\rangle \text{d}(|V|C)$ for HSE (**c**) and DD (**d**). For experiments analyzed by finding the slope of curves such as those in Figs. 12 and 13, (**c**, **d**) are appropriate

4.3 Experimental Results

Figure 8a shows an EPR spectrum of 5-mM 15NH in 60%AG at273 K, and the lf- and hf-manifolds, Fig. 8b, c, respectively, on an expanded abscissa by omitting 13 G. This is not a spectrum that we include in the analysis because it is not

Integrated Intensity
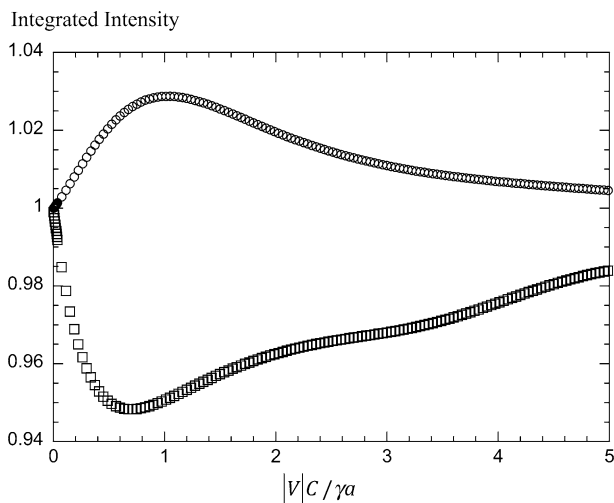
Fig. 7 The apparent doubly integrated intensity Eqs. (18) and (34) of Ref. [20] normalized at $c = 0$ for HSE, circles, and DD, squares. The true doubly integrated intensity is constant, but the presence of the intra-manifold dispersions distorts the values of both ΔH^0_{ppM} and V^{man}_{ppM} while maintaining the line shape. The values of ΔH^0_{ppM} are too large and V^{man}_{ppM} too small, resulting in apparent doubly integrated intensities only 3% too large for HSE and 5% too small for DD

unresolved; however, it serves to clarify our terminology. We refer to spectra such as Fig. 8b as partially resolved and such as Fig. 8c as showing incipient resolution. These qualitative descriptions are quantified by the value of χ_M; for Fig. 8b $\chi_{lf} = 3.0$ and for Fig. 8c, $\chi_{hf} = 2.4$. In Fig. 8b, c, the overlying traces are the residuals between the experimental spectrum and the fit to Eq. (44), showing narrow lines indicative of incipient resolution; the more resolved, the larger are these lines. We show some data in this paper for partially resolved manifolds; however, our analysis is restricted to values of $\chi < 2.3$.

Figure 9a displays an EPR spectrum of 12-mM 15ND in 60 wt% aqueous glycerol at 273 K, Fig. 9b the residuals amplified by 10, Fig. 9c the dispersion component of the fit amplified by a factor of 10, and Fig. 9d the absorption component of the fit. The residuals are composed mostly of an [14]N Tempol impurity, the small, center line and two of the outer lines, and 8 lines due to ^{13}C in natural abundance. The smaller innermost lines, closely spaced, for the lf-manifold, $\chi_{lf} = 0.70$, are due to the inherent resolution in the unresolved spectrum. These are not evident in the hf-manifold because of the lower value of $\chi_{hf} = 0.32$. The dispersion components for lf are negative, indicative of DD spectra; they are not proportional in height to the lines in 7d because of instrumental dispersion. Spectra of 15 HD at all concentrations and temperatures are unresolved.

Figure 10 shows a spectrum of 12-mM 15NH in 60%AG at 273 K with an amplification of 2.5 relative to Fig. 9. The impurity line due to 14NH is evident in the center of the spectrum; however, the ^{13}C lines are now dominated by the inherent proton resolution in the unresolved spectrum. These residuals are expected
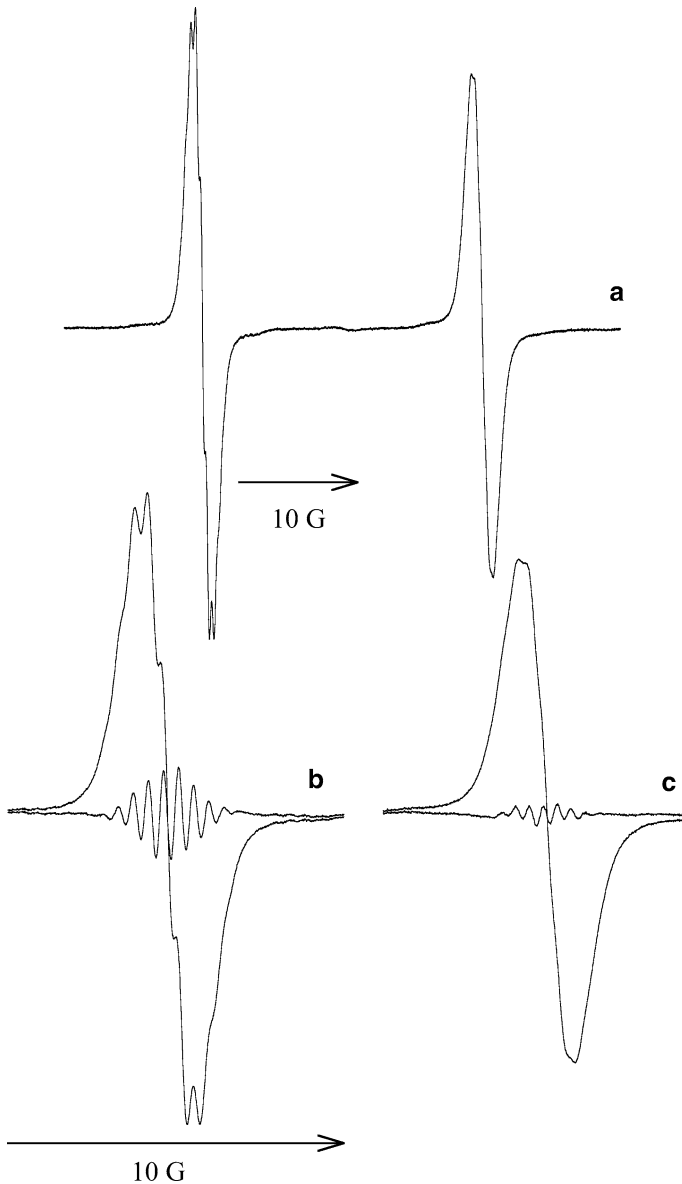
Fig. 8 **a** EPR spectrum of 5 mM ^{15}N-Tempol-H in 60% aqueous glycerol at 298 K, **b** lf-, and **c** hf manifolds, respectively, with the central 13 G omitted. In **b**, **c**, the overlying traces are the residuals between the experimental spectrum and the fit to Eq. (44), showing narrow lines indicative of incipient resolution; the more resolved, the larger are these lines

because of the relatively high values of $\chi_{lf} = 1.8$ and $\chi_{hf} = 1.2$, for lf and hf, respectively.

Figure 11 displays values of ΔH_{pplf}^{man} and $\langle \Delta H_{pplf}^{L} \rangle$ at 340 K for 15NH, Fig. 11a and 15 ND, Fig. 11b and at 273 K for 15 NH, Fig. 11c and 15 ND, Fig. 11d. The
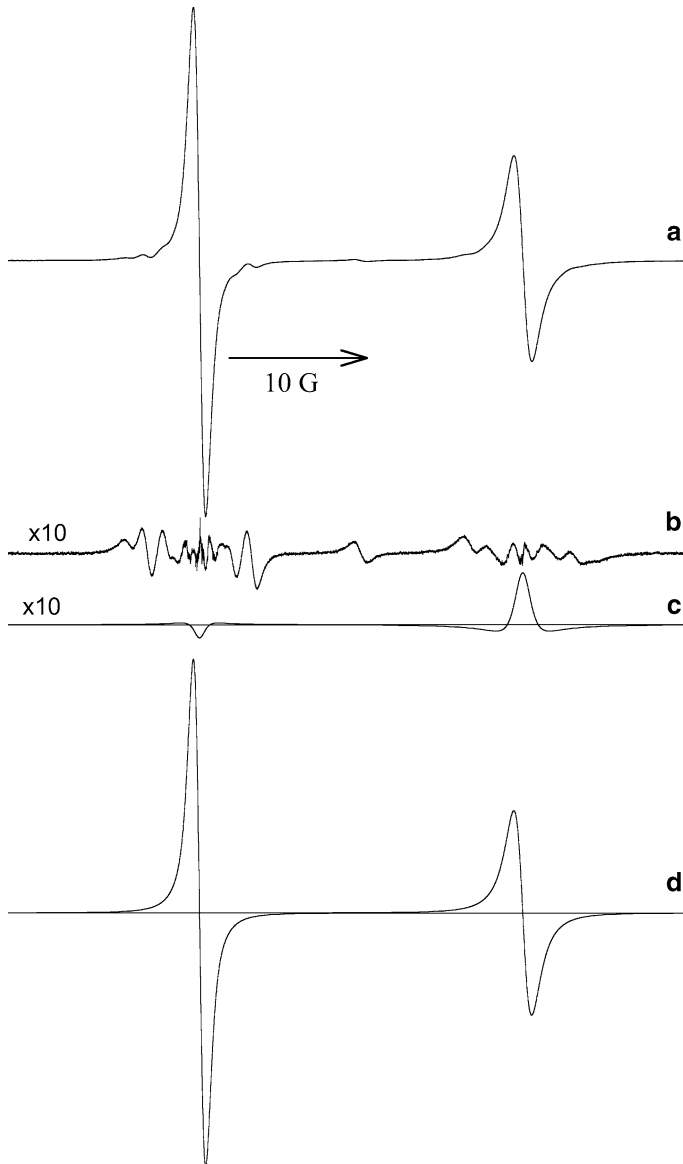
Fig. 9 **a** EPR spectrum of 12 mM 15 ND in 60 wt% aqueous glycerol at 273 K, **b** the residual amplified by 10, **c** the dispersion component of the fit amplified by a factor of 10, and **d** the absorption component of the fit. The residual is composed mostly of an [14]N Tempol impurity, the inner line and two outer lines, and 8 lines due to ^{13}C in natural abundance. The smaller innermost lines, closely spaced, are due to the mismatch between the Voigt shape and the experimental spectrum. The dispersion lines are negative, typical of DD spectra; they are not proportional in height to the lines in **d** because of instrumental dispersion
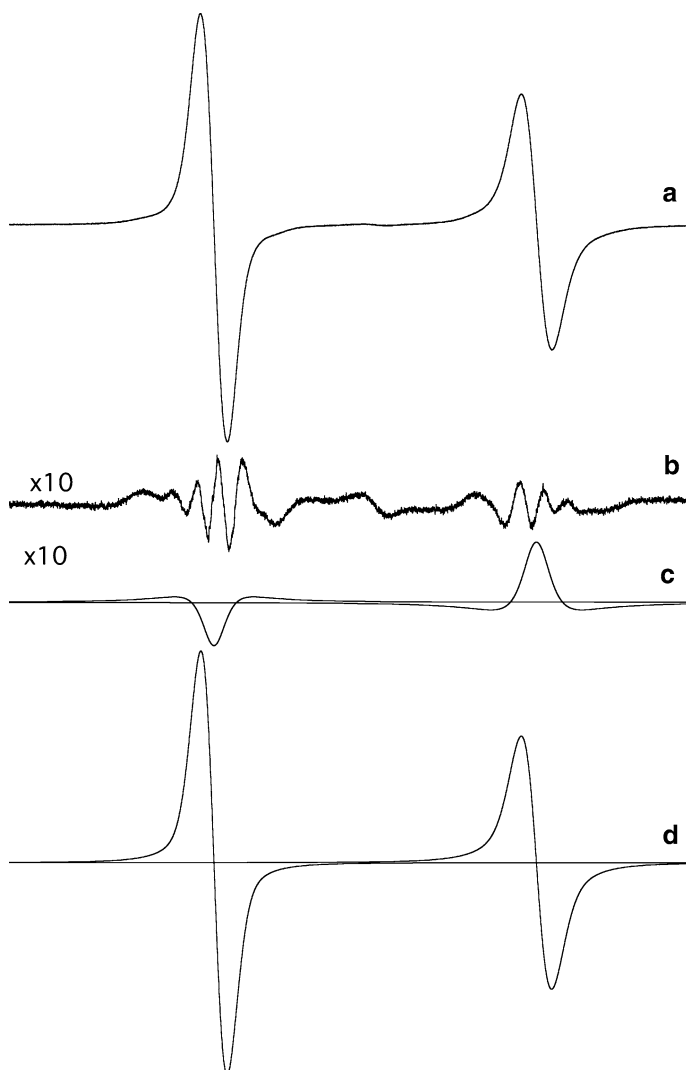
Fig. 10 a EPR spectrum of 12 mM ^{15}N protonated Tempol in 60 wt% aqueous glycerol at 273 K at a relative amplification of 2.5 relative to Fig. 1. See the caption of Fig. 9 for a description of **b–d**. The residual in this case, in addition to ^{15}N and ^{13}C lines, shows more intense lines in the center of each manifold due to incipient resolution due to proton hyperfine coupling

results from Figs. 9 and 10 are indicated by the vertical arrows. For those spectra, $\Delta H_{\text{pplf}}^{\text{man}}$ is larger than $\Delta H_{\text{pplf}}^{\text{L(Voigt)}}$ by 125 and 32% for 15 NH and 15 ND, respectively; thus, a considerably larger correction is required for 15 NH and the residuals are considerably larger. Nevertheless, the slope of $\Delta H_{\text{pplf}}^{\text{L(Voigt)}}$ for the two isotopes are within 2.6% of the mean value of 38.5 G/M. The need for correction for IHB is mitigated by deuteration but, for careful work, is not eliminated. Slopes of the straight lines yield $B' \equiv \mathrm{d}\Delta H_{\text{pplf}}^{\text{L(Voigt)}}/\mathrm{d}C$ and the intercepts $\Delta H_{\text{pplf}}^{\text{L}}(0)$. These slopes
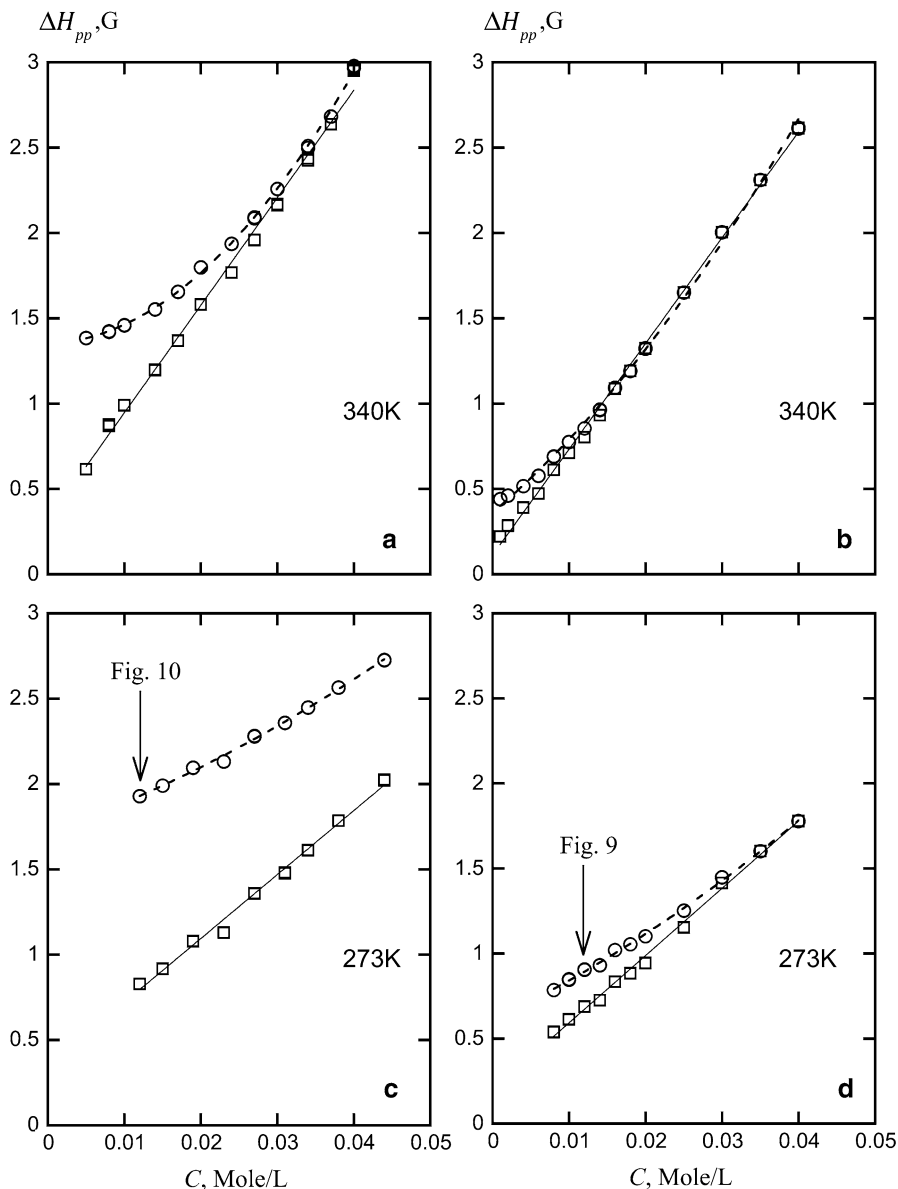
Fig. 11 Peak-to peak line widths of the lf manifold, $\Delta H_{\mathrm{pplf}}^{\mathrm{man}}$, circles, and $\Delta H_{\mathrm{pplf}}^{\mathrm{L(Voigt)}}$, squares. **a** 15 NH, 340 K; **b** 15 ND, 340 K; **c** 15 NH, 273 K; **d** 15 ND, 273 K. The straight line is a least-square fit to d $\Delta H_{\mathrm{pplf}}^{\mathrm{L(Voigt)}}$ and the dashed line a quadratic fit to $\Delta H_{\mathrm{pplf}}^{\mathrm{man}}$ to guide the eye. The vertical arrows indicate the spectra in Figs. 9 and 10, respectively. For those spectra, $\Delta H_{\mathrm{pplf}}^{\mathrm{man}}$ is larger than $\Delta H_{\mathrm{pplf}}^{\mathrm{L(Voigt)}}$ by 125 and 32% for 15 NH and 15 ND, respectively; thus, a considerably larger correction is required for 15 NH and the residuals are considerably larger. Nevertheless, the slope of $\Delta H_{\mathrm{pp-1/2}}^{\mathrm{L(Voigt)}}$ for the two isotopes are within 2.6% of the mean value of $B' = 38.5$ G/M

and intercepts together with those from the other manifolds (not shown) are averaged and given in Tables 6, 7, 8 and 9.

Figure 12a is a plot of V_{displf}/V_{pplf} for 15 NH (open symbols) and 15ND (closed symbols) at 340 K (squares), 298 (circles), and 273 K (diamonds) corrected for instrumental dispersion. Figure 12b Shows values of V_{displf}/V_{pplf} (open symbols)

Table 6 Rate constants 15 NH

T (K)	k^a	B'^a (G/M)	K_{ex}/γ^a (G/M)	W_{dd}/γ^a (G/M)	V^b (M^{-1})	K_{ex}/γ^b (G/M)	W_{dd}/γ^b (G/M)
273	-0.03 ± 0.03	37.0 ± 1.4	13.2 ± 1.2	25.4 ± 1.1	0.717 ± 0.96	15.4 ± 2	24.4 ± 1.7
298	0.50 ± 0.03	44.4 ± 1.2	39.7 ± 1.7	18.6 ± 0.8	15.9 ± 1.2	41.8 ± 2	17.5 ± 1.7
323	1.04 ± 0.03	49.4 ± 1.0	71.1 ± 2.1	7.3 ± 0.8	35.3 ± 1.5	73.9 ± 3	5.85 ± 1.8
333	1.14 ± 0.03	55.3 ± 0.7	85.1 ± 2.1	5.4 ± 0.9	43.2 ± 1.8	88.5 ± 3	3.64 ± 1.8
340	1.25 ± 0.03	63.1 ± 1.1	104 ± 2.7	2.7 ± 1.0	55.3 ± 2.2	110 ± 4	-0.511 ± 2.5

W_{dd} for ^{15}N may be compared with that for ^{14}N by multiplying by 21/19 for the HVL or 15/14 for the LVL. [18]

[a]Derived from fitting

[b]Derived from the two-point method

Table 7 Rate constants 15 ND

T (K)	k^a	B'^a (G/M)	K_{ex}/γ^a (G/M)	W_{dd}/γ^a (G/M)	V^b (M^{-1})	K_{ex}/γ^b (G/M)	W_{dd}/γ^b (G/M)
273	-0.05 ± 0.03	36.7 ± 1.3	12.4 ± 1.2	25.6 ± 1.1	-1.05 ± 0.89	12.5 ± 2	25.5 ± 1.6
298	0.50 ± 0.03	41.0 ± 1.0	36.7 ± 1.7	17.2 ± 0.8	15.2 ± 0.84	39.5 ± 2	15.8 ± 1.4
323	0.99 ± 0.03	50.9 ± 0.6	70.3 ± 1.7	8.9 ± 0.7	36.5 ± 1.1	76.4 ± 2	5.89 ± 1.3
333	1.10 ± 0.03	57.7 ± 0.6	86.1 ± 1.9	6.9 ± 0.8	46.4 ± 1.1	94.4 ± 2	2.76 ± 1.3
340	1.14 ± 0.03	61.9 ± 0.7	94.9 ± 2.1	6.1 ± 0.9	51.7 ± 1.3	104 ± 2	1.48 ± 1.5

W_{dd} for ^{15}N may be compared with that for ^{14}N by multiplying by 21/19 for the HVL or 15/14 for the LVL [18]

[a]Derived from fitting

[b]Derived from the two-point method

Table 8 Rate constants 14 NH

T (K)	k^a	B'^a (G/M)	K_{ex}/γ^a (G/M)	W_{dd}/γ^a (G/M)	V^b (M^{-1})	K_{ex}/γ^b (G/M)	W_{dd}/γ^b (G/M)
273	0.13 ± 0.04	34.0 ± 0.6	17.1 ± 1.2	18.0 ± 0.9	-0.3 ± 6	12 ± 14	21 ± 5
298	0.57 ± 0.02	43.8 ± 0.7	39.7 ± 0.9	11.5 ± 0.47	7.1 ± 5.3	32 ± 11	17 ± 5
323	0.90 ± 0.02	55.8 ± 0.6	67.5 ± 1.5	3.31 ± 0.84	17 ± 6	56 ± 12	11 ± 5
333	0.97 ± 0.01	63.0 ± 0.8	79.9 ± 1.3	1.3 ± 0.5	23 ± 5	73 ± 11	6 ± 5
340	0.13 ± 0.04	34.0 ± 0.6	87.6 ± 1.9	0.7 ± 1.1	28 ± 7	86 ± 15	2 ± 6

[a]Derived from fitting

[b]Derived from the two-point method

Table 9 Rate constants 14 NHΣ

T (K)	k^a	B'^a (G/M)	K_{ex}/γ^a (G/M)	W_{dd}/γ^a (G/M)	V^b (M^{-1})	K_{ex}/γ^b (G/M)	W_{dd}/γ^b (G/M)
273	0.08 ± 0.01	36.6 ± 0.6	16.6 ± 0.6	20.6 ± 0.5	2.1 ± 1.0	19 ± 2	19 ± 1
298	0.55 ± 0.01	46.2 ± 0.5	41.0 ± 0.7	12.7 ± 0.4	10.7 ± 0.6	40 ± 1	13 ± 1
323	0.89 ± 0.02	60.8 ± 0.7	72.6 ± 1.3	4.23 ± 0.7	22.9 ± 0.9	72 ± 2	5 ± 2
333	0.937 ± 0.014	69.8 ± 0.7	86.6 ± 1.2	2.68 ± 0.6	30 ± 2	90 ± 4	0.3 ± 1.9
340	0.97 ± 0.020	77.4 ± 0.7	98.3 ± 1.7	1.51 ± 1.0	30 ± 2	94 ± 4	5 ± 2

[a] Derived from fitting

[b] Derived from the two-point method
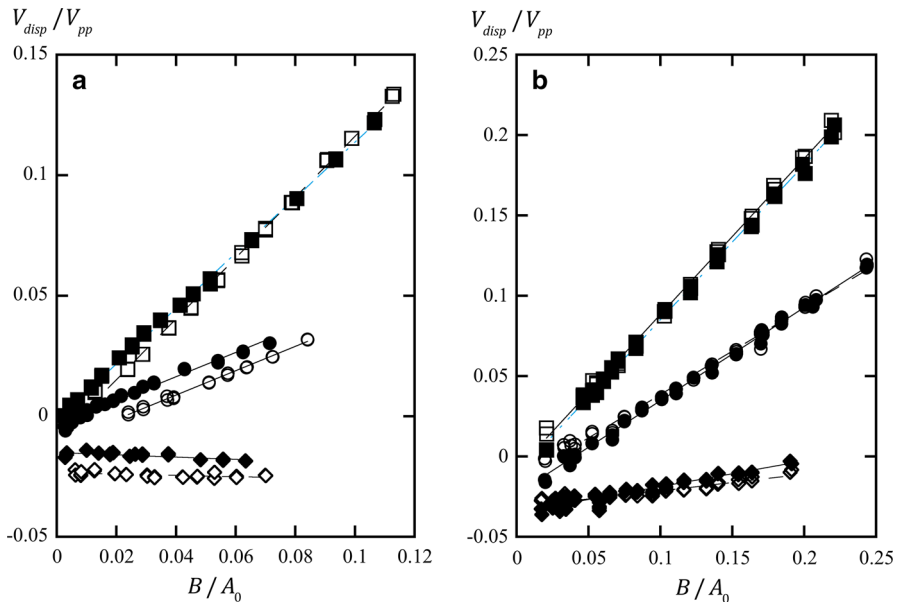
Fig. 12 **a** V_{displf}/V_{pplf} for 15 NH (open symbols) and 15 ND (closed symbols) at 340 K (squares), 298 (circles), and 273 K (triangles) corrected for instrumental dispersion. **b** V_{displf}/V_{pplf} (open symbols) and $-V_{disphf}/V_{pphf}$ (closed symbols) for 14 NH. These values have been corrected using Eq. (49); however, except for 273 K, the corrections are smaller than the symbols. The data vary linearly with the normalized broadening, B/A_0; however, do not extrapolate to the origin, especially at 273 K

and $-V_{disphf}/V_{pphf}$ (closed symbols) for 14 NH. These values have been corrected from fitted values using Eq. (49); however, except for 273 K, the corrections are smaller than the symbols. The data vary linearly with the normalized broadening, B/A_0; however, do not extrapolate to the origin, especially at 273 K. We have observed this phenomenon in the past [31] and have rationalized it by simulating $C \rightarrow 0$ spectra including the pseudo-secular electron–nuclear dipolar interaction. We observed (see Fig. 4 of the Supplemental Information of Ref. [31]) spectra characteristic of transfer of spin coherence with negative values of V_{displf}/V_{pplf}. Marsh [35] has since demonstrated that such transfer occurs in the absence of HSE

or DD; thus, it is correct to find the slopes ^{14}k and ^{15}k without constraining the fits to the origin.

The slopes of the straight lines, ^{14}k or ^{15}k, and the intercepts are given in Tables 6, 7, 8 and 9 together with the rate constants computed from ^{A}k and $^{A}B'$.

Figure 12 demonstrates two interesting points: (1) the intercepts show a systematic difference for protons vs deuterons (Fig. 12a) and (2) (Fig. 12b) the lf- and hf-manifolds show the same intercept as is necessary for transfer of spin coherence due to the pseudo-secular electron–nuclear dipolar interaction.

Figure 13a shows values of $-p_{\text{lf}}{}^{15}A_0/2$ for the lf of 15NH, open symbols, and for 15ND, closed symbols, at temperatures 273 K (diamonds), 298 K (circles), and 340 K, (squares), for the same data as those in Fig. 12. Figure 13b shows values of $-p_{\text{lf}}{}^{14}A_0/3$ (open symbols) and $+p_{\text{hf}}{}^{14}A_0/3$ (closed symbols) for 14NH. Unlike the plots in Fig. 12, these deviate from linearity as C increases because of overlap with adjacent lines. To mitigate this problem, we have only fit values that satisfy $A_0/\Delta H_{\text{ppM}}^{\text{man}} \geq 7$. All of the data for ^{15}N satisfy this criterion, while most do not for ^{14}N. The straight lines fit to the data in 13b that satisfy this criterion are extended to the limits of the plot for clarity, but only the lower values of C are fit. Values of the slopes of these straight lines, V, are given in Tables 6, 7, 8 and 9. As expected, because $^{14}A_0$ is smaller by a factor of 1.403, [29] the overlap becomes a problem in general at lower values of C for ^{14}N. Notable in Fig. 13b is the fact that the lf and hf
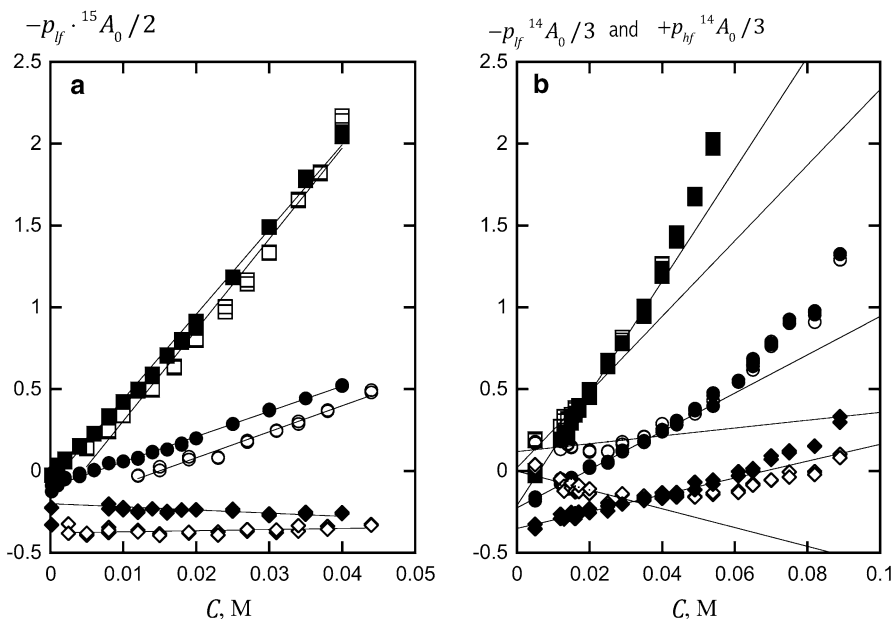

Fig. 13 a Values of $-p_{\text{lf}}{}^{15}A_0/2$ for the lf of 15 NH, open symbols, and for 15ND, closed symbols, at temperatures 273 K (diamonds), 298 K (circles), and 340 K, (squares), for the same data as those in Fig. 12. **b** shows values of $-p_{\text{lf}}{}^{14}A_0/3$ (open symbols) and $+p_{\text{hf}}{}^{14}A_0/3$ (closed symbols) for 14NH. Unlike the plots in Fig. 12, these deviate from linearity as C increases because of overlap with adjacent lines
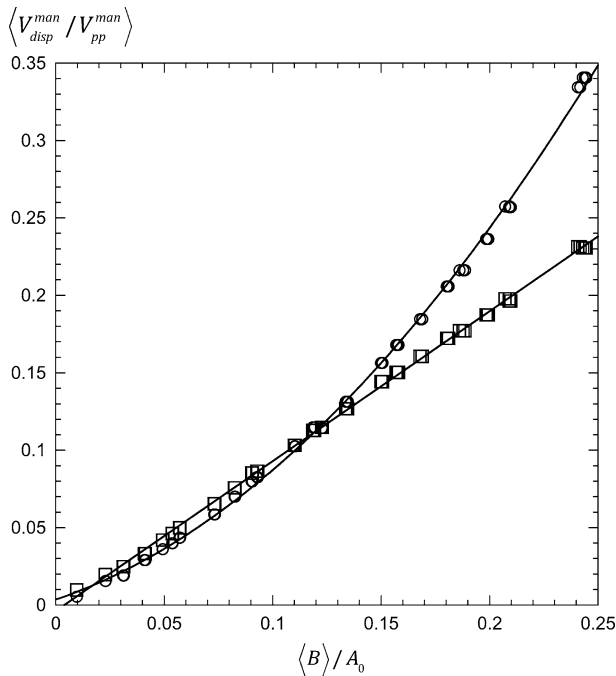
$$\left\langle V_{disp}^{man} / V_{pp}^{man} \right\rangle$$

Fig. 14 Relative dispersion amplitude as derived from the two-point method, circles, and from fitting, squares for 14 NHΣ at 340 K. $\langle V_{disp}^{man} / V_{disp}^{man} \rangle$ is the average over the lf- and hf-manifolds, and B is the average over all three lines. The multiple points are from different runs of the same sample to show the reproducibility. The straight line is a fit to Eq. (62) yielding $k = 0.968$ and the curved line is a quadratic to guide the eye through the circles

results are significantly different, especially at 273 K. This difference is expected if there is an underlying impurity line, and, in fact, we show in "Appendix 3" that this is the case. Figure 12b shows that the slopes of the *lf* and *hf* lines by the fitting method differ by considerably less.

Figure 14 shows a direct comparison between the fitting method, squares, and the two-point method, circles, for 14 NHΣ taken at 340 K. The two parameters are placed on the same footing using Eq. (62). The values of $\langle V_{dispM}^{man} / V_{ppM}^{man} \rangle$ are averages over the lf- and hf-manifolds, and $<B>$ the average broadening over all three lines. The multiple points are from different runs of the same sample to show the reproducibility. The straight line is a fit to Eq. (54) yielding $k = 0.968$ and the curved line is a quadratic to guide the eye through the circles.

5 Discussion

Finding values of K_{ex} and W_{dd} from an experimental spectrum in the proton dark zone relies on obtaining accurate values of the average Lorentzian line width of the unresolved IHB manifolds, $\langle \Delta H_{ppM}^{L} \rangle$, and the average value of the dispersion to

absorption ratio, $\langle V_{\text{disp}M}/V_{\text{pp}M}\rangle$. Assumption 1 asserts that the former may be obtained by extracting $\Delta H_{\text{pp}M}^{\text{L(Voigt)}}$ by fitting the manifold to a Voigt. Assumption 2 states that the latter may be obtained from either a Voigt fit value of $V_{\text{disp}M}^{\text{man}}/V_{\text{disp}M}^{\text{man}}$ transformed by Eq. (49), or by measuring p_M from the asymmetry of the spectrum according to Eq. (60).

This paper reaffirms that $\Delta H_{\text{pp}M}^{\text{L(Voigt)}}$ is equal to $\langle\Delta H_{\text{pp}M}^{\text{L}}\rangle$ to remarkable precision using several sources of information. (1) Fitting the perturbation result in Fig. 1 yields errors within 2% for either HSE or DD despite the interference of the intra-manifold dispersions. Thus, assumption 1 holds in the heart of the dark zone. (2) Values of $B_M' = \mathrm{d}\Delta H_{\text{pp}M}^{\text{L(Voigt)}}/\mathrm{d}C$ as $C \to 0$ agree with the values from Eqs. (36) and (42) for HSE or DD, respectively. See the insets to Figs. 2 and 3. (3) Experimentally, we find excellent agreement between the values of B_M' derived from 15 NH versus 15ND. For example, compare Fig. 9c, d at 273 K. $B_{\text{lf}}' = 36.2 \pm 0.6$ G/M for 15 NH and 37.1 ± 0.7 G/M. For the hf manifold (not shown in Fig. 9), the comparison is $B_{\text{lf}}' = 37.8 \pm 0.6$ G/M for 15NH and 37.2 ± 0.7 G/M. This agreement is fortuitous as shown by comparing the results of the two isotopes at other temperatures in Table 7. Nevertheless, in view of the fact that the manifold line widths must be corrected by up to 125% and 32% for 15NH and 15ND, respectively; this is a remarkable result that clearly demonstrates the accuracy of determining Lorentzian line widths in IHB spectra. Assumption 1 rests on the fact that spectra undergoing HSE and/or DD remain good Voigts, "Appendix 2". Fitting unresolved manifolds of complicated spin modes must be considered a phenomenological procedure, but one that is useful and accurate.

Assumption (2) is less accurate in the proton dark zone as evidenced by Figs. 5 and 6. For HSE, the error in the slope, (c), varies from 28 to 0% for $|V|C/\gamma a = 0$–1.3 from the two-point method, while fitting yields errors from 33 to 5% over that same range. For $|V|C/\gamma a > 1.3$, the two-point method rapidly deteriorates, while fitting yields results within 1–2% over the entire range. For DD, the error in the slope, (d), varies from 32 to 20% for $|V|C/\gamma a = 0$–0.7 from the two-point method and rapidly deteriorates at higher values of $|V|C/\gamma a$. Fitting yields errors from 37 to 0% for $|V|C/\gamma a = 0$–1.3; above this fitting yields results within 5% at worst and near zero on average, depending on how large a value of for $|V|C/\gamma a$ is employed in the fit. From [17], it appeared that the two-point method would be suitable for larger values of VC; however, in practice, line overlap prevails.

Comparing the resulting rate constants in Tables 6, 7 and 8, we find generally good agreement between the two-point method and fitting; however, some of this agreement may be fortuitous because both methods show similar errors through the proton dark zone. Referring to the particular case of Fig. 14, where the two-point method yields results closer to a quadratic than a linear dependence, the result depends on the regions selected to fit to a straight line. The final row of Table 9 shows that the final results are in rather good agreement, but one needs to keep in mind that the quoted errors are random and systematic errors and do not include any estimate of the error due to the range fit.

At our present state of knowledge, we cannot elaborate very much on the details of the proton dark zone because we do not yet have a detailed theory for 13 lines like we do for 2, 3, or 5 lines numerically [13], or 2 or 3 lines, analytically [5]; however, we may use these latter results to guide our thinking. Figure 15 shows results for the
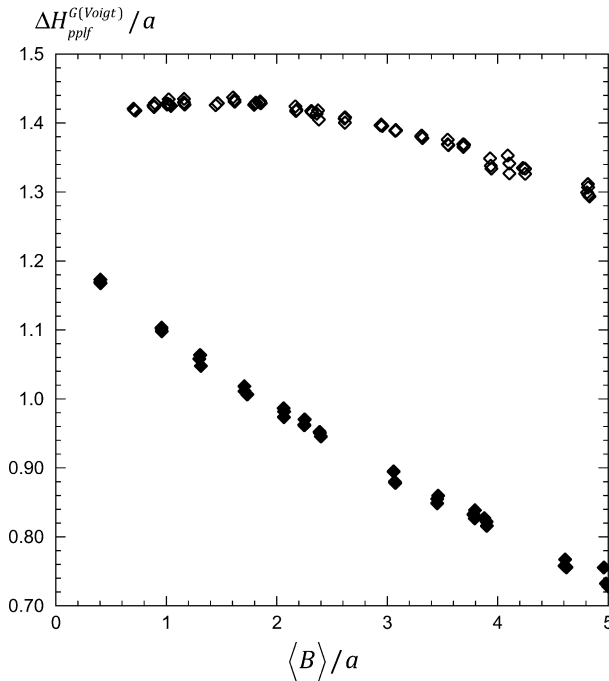
Fig. 15 Experimental Gaussian line widths for the lf-manifold of 14 NHΣ at 273 K, open diamonds, and 340 K, closed diamonds. Compare the general behavior of these with those of Figs. 3 and 4 where $\Delta H_{\text{pp}M}^{\text{G(Voigt)}}$ decreases rapidly for HSE and increases slightly before decreasing for DD, respectively

experimental Gaussian line widths for the lf-manifold of 14NH Σ at 273 K, open diamonds, and 340 K, closed diamonds. Compare the general behavior of these with those of Figs. 3 and 4 where $\Delta H_{\text{pp}M}^{\text{G(Voigt)}}$ decreases rapidly for HSE and increases slightly before decreasing for DD, respectively. From Eq. (31), we know that the proton lines within a manifold move toward the center equally for HSE and DD. This contributes to a decrease in the second moment detected as a decrease in $\Delta H_{\text{pp}M}^{\text{G(Voigt)}}$. If the height of the proton lines remained the same, then $\Delta H_{\text{pp}M}^{\text{G(Voigt)}}$ would decrease at the same rate, but they do not remain the same. For HSE, the outer lines broaden the most, decreasing the relative heights of the outer lines according to Eq. (15). This effect lowers the value of the second moment calculated from $\sigma^2 = \sum V_{\text{pp}mM}(H_{mM})^2$. In contrast, for DD, the outer lines broaden the least, increasing their relative heights leading to an increase in σ^2. This increase is eventually overcome by the effect of the collapsing proton structure, so one expects to observe an initial increase followed by a decrease. For 2–5 lines, there is another effect in the case of HSE that accelerates the decrease in $\Delta H_{\text{pp}M}^{\text{G(Voigt)}}$, namely that the outer lines actually lose intensity to the inner lines and even eventually go into emission; that is to say that the intensities become negative [5, 13]. This has a profound effect on the decrease in $\Delta H_{\text{pp}M}^{\text{G(Voigt)}}$ that may signal a similar behavior in 13 lines.

The presence of the intra-manifold dispersions may be detected as an increase (HSE) or a decrease (DD) in the doubly integrated intensity (Fig. 7); however, in the

present experiment this effect falls within the scatter of the data. Similarly, the presence of the intra-manifold dispersion lead to rather large errors through the dark zone (Figs. 5, 6).

An interesting result of the present work, shown in Fig. 12, is that the values of $V_{\text{displlf}}/V_{\text{pplf}}$ for $C \rightarrow 0$ are different for protons and deuterons. This is an effect that we have not seen in the past because this is the first time protonated vs. deuterated nitroxides have been studied in the same experiment. Because Marsh [35], treating the case without IHB, has shown that non-zero intercepts are expected this new finding may offer interesting insights into the role of the proton or deuteron interactions on the relaxation processes. He has predicted the difference between ^{14}N and ^{15}N.

6 Conclusions

By studying ^{14}N and ^{15}N, the latter protonated or deuterated, we conclude the following:

1. The rate constants describing HSE and DD are in reasonable agreement for the two isotopes, deuterated or protonated employing either the fitting and two-point methods; however, generally smaller error bars are found with the fitting method. Tables 6, 7, 8 and 9. These rate constant show dependences on T/η, similar to those for per-deuterated ^{14}N and ^{15}N Tempone in 70 wt% aqueous glycerol [18].
2. Assumption 1, that the average Lorentzian line width is well approximated by the Voigt Lorentzian line width is confirmed both experimentally (comparing 15 NH and 15 ND) and theoretically from fits to spectra computed with perturbation theory and from the $C \rightarrow 0$ behavior of spectra simulated from the exact Eq. (1).
3. An interesting difference in the behavior of the intercepts for protonated and deuterated nitroxides as $C \rightarrow 0$ was discover experimentally that does not yet have an explanation.
4. For experiments that are carried out with protonated nitroxides, the separation of HSE and DD carries errors up to 10–30% for low concentrations and small values of T/η depending on the range of concentrations used. In many cases, this situation may be improved by deuteration and using higher concentrations; however, in limited cases such as Refs. [28, 36], higher concentrations may not be an option. If higher concentrations are employed, then only the fitting method will be applicable. Failing to design an experiment that avoids low concentrations with a nitroxide that is not cost-prohibitive to deuterate, one might have to resort to finding procedures to correct the measured values of $\langle V_{\text{disp}M}^{\text{man}}/V_{\text{disp}M}^{\text{man}} \rangle$ such that they agree with simulated values of $V_{\text{disp}M}/V_{\text{pp}M}$; i.e., correct the curves in the inset to Fig. 5 such that $\langle V_{\text{disp}M}/V_{\text{pp}M} \rangle$ and $V_{\text{disp}M}^{\text{man}}/V_{\text{disp}M}^{\text{man}}$ coincide.

# Appendix 1: Exaggerated Values of $\langle V_{\text{disp}M}/V_{\text{pp}M}\rangle$

Figure 16 shows thirteen Lorentzian absorptions (a) and inter-manifold dispersions (b) of binomial relative intensities, light lines, and the sums, bold lines. (c) The sum of the absorption and dispersion manifolds. On this scale, there appear to be 9 lines because the outer 4 are not observable. Compare with Fig. 1, except the intra-manifold dispersions are not shown and a greatly exaggerated value of $\langle V_{\text{disp}M}/V_{\text{pp}M}\rangle = 0.3$ is employed to emphasize the asymmetry of the spectrum. The lf- and hf-manifolds are spaced by the ^{15}N hyperfine coupling constant,
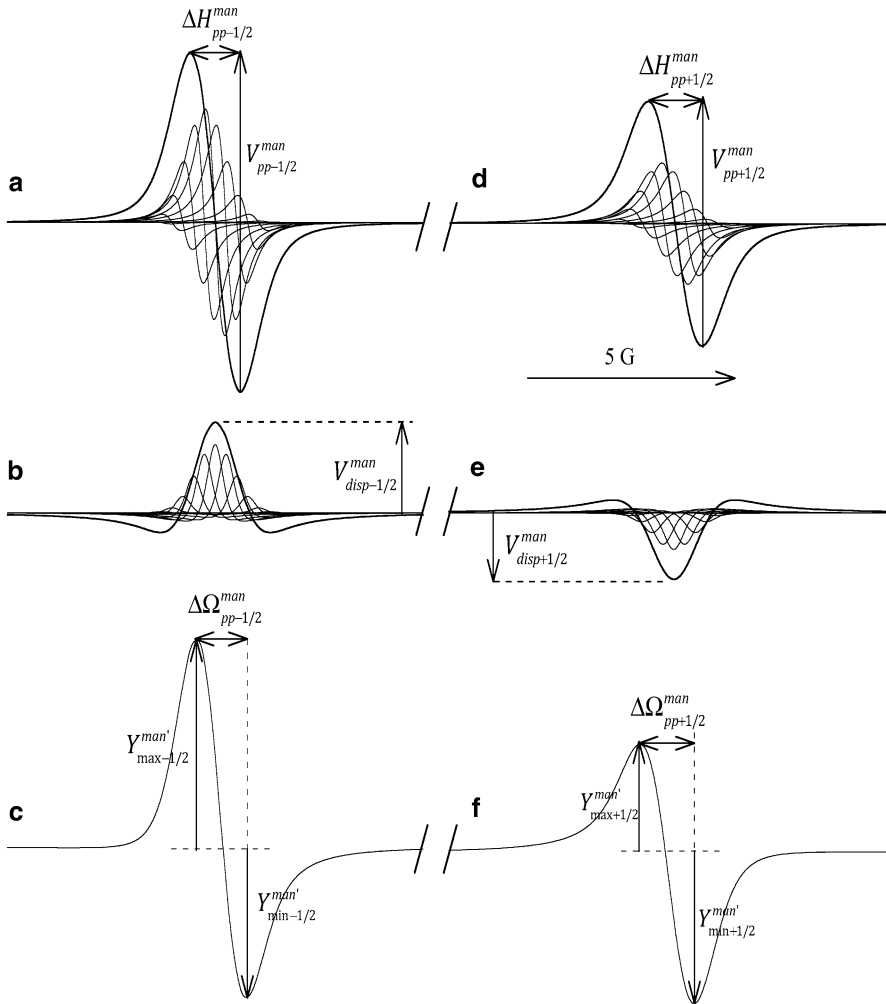
Fig. 16 a Thirteen Lorentzian absorptions and **b** inter-manifold dispersions of binomial relative intensities, light lines, and the sums, bold lines. **c** The sum of the absorption and dispersion manifolds. On this scale, there appear to be 9 lines because the outer 4 are not observable
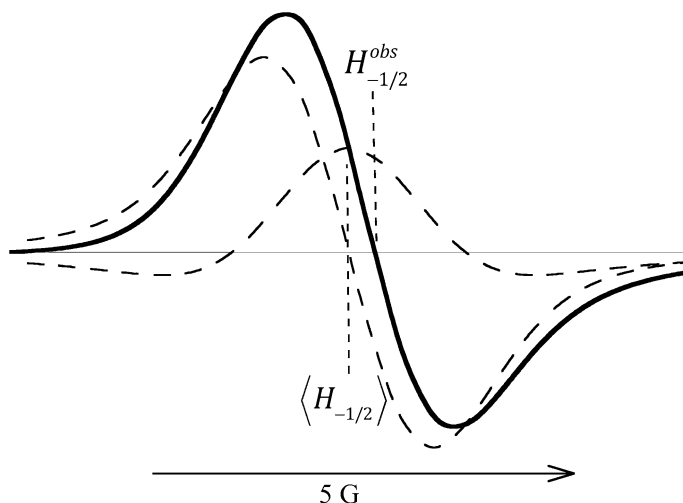
Fig. 17 The lf-manifold of Fig. 16 showing the resonance field, $H_{-1/2}$ and where the admixture crosses the baseline

$A_0 = 22.0$ G; however, the central 12 G of each trace has been removed to emphasize the structure; thus, the nitrogen spacing is about twice as large as it appears. The intrinsic Lorentzian line widths for the two manifolds are $\Delta H_{pp+1}^L = 0.4680$ G and $\Delta H_{pp-1}^L = 0.6521$ G, respectively, and $a = 0.26$ G. The absorption–dispersion admixtures (c) and (f) are asymmetric, reminiscent of line shapes that are now familiar for nitroxides undergoing HSE; e.g., Figure 9a of Ref. [23, #3822]. Of course, in this latter case, the IHB will have collapsed, so the manifolds are effectively Lorentzian, in contrast with Fig. 16. The quantities $\Delta \Omega_{ppM}^{man}$, $Y_{maxM}^{man'}$, and $Y_{minM}^{man'}$ are defined.

The resulting manifolds have $V_{disp}^{man}/V_{pp}^{man} = 0.2675$ (lf) and 0.2708 (lf), 11 and 10% smaller than V_{dispM}/V_{ppM}, respectively. When transformed by Eq. (49), $\langle V_{disp}^{man}/V_{pp}^{man} \rangle = 0.300$ for both manifolds.

Figure 17 shows the low-field line of the admixture, Fig. 1c, on an expanded scale showing the resonance field, H_{lf}^{abs}; i.e., where the absorption crosses the baseline (where the dispersion is maximum); and where the admixture crosses the baseline, H_{lf}^{obs}. In this case, in which the lf-manifold is positive because HSE dominates, H_{lf}^{obs} is up field from $\langle H_{-1/2} \rangle$; the opposite is true at hf, so the separation between the two admixtures, A_{obs}, is less than between the resonance frequencies, A_{abs}. For DD, the reverse occurs. See Fig. 11a of Ref. [11] for an experimental example of an increasing A_{obs} as C increases.

Figure 18 shows values of $V_{disp}^{man}/V_{pp}^{man}$ derived by the two methods as a function of χ_M.

$$\frac{V^{man}_{dispM}}{V^{man}_{ppM}} \Bigg/ \left\langle \frac{V_{dispM}}{V_{ppM}} \right\rangle$$
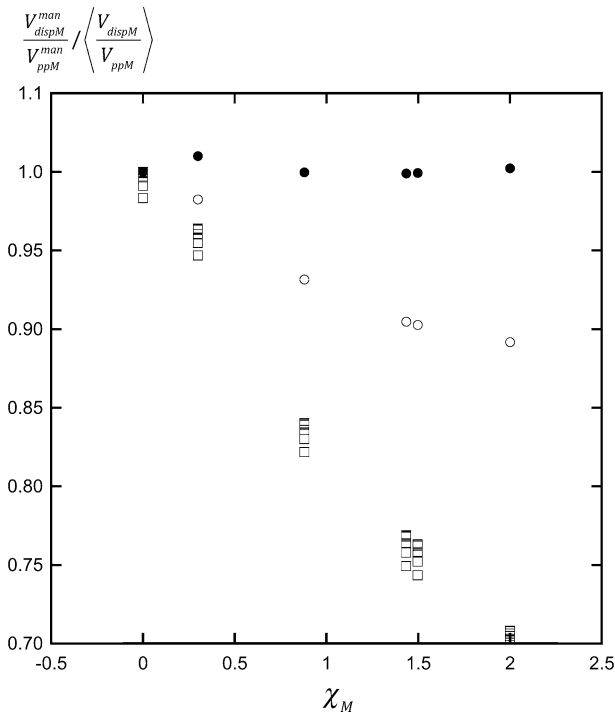

Fig. 18 Values of $V^{man}_{dispM}/V^{man}_{ppM}$ from fitting, open circles, and from the two-point method, open squares as functions of χ_M. The closed circles are obtained from the open circles by applying the correction Eq. (49). For input values of $\langle V_{dispM}/V_{ppM} \rangle$ ranging from 0 to 0.4, the fitting method yields the same value, while the two-point method yields somewhat different values as shown by the scatter of the open squares

Appendix 2: IHB Spectra Remain Excellent Voigt Line Shapes Under HSE or DD

Spectra were generated for HSE and DD with Eq. (1) and for $C = 0$ from Ref. [23, #3822]. The input parameters are given in the caption to Fig. 16. The spectra were fit with Eq. (44) and the differences between the fit and the spectra, the residuals, were computed. Figure 19 shows the lf-manifold of spectra and the resulting residuals for conditions near and including incipient resolution. The $C = 0$ spectra were computed by holding the proton spacing constant at $a = 0.4$ G and varying ΔH^{L}_{pp} such that the range of $\chi_{-1/2}$ overlapped that of the HSE and DD results.

Figure 20 shows the maximum value of the residuals, R_{max}, as a fraction of V^{man}_{pplf}. This plot shows that for $\chi_{-1/2} < 2$, the difference in the Voigt shape and the spectrum is 1% or less; thus, for all three cases, HSE, DD, and $C = 0$, the spectra are accurately modelled as Voigt shapes. For the hf-manifolds of all spectra, with
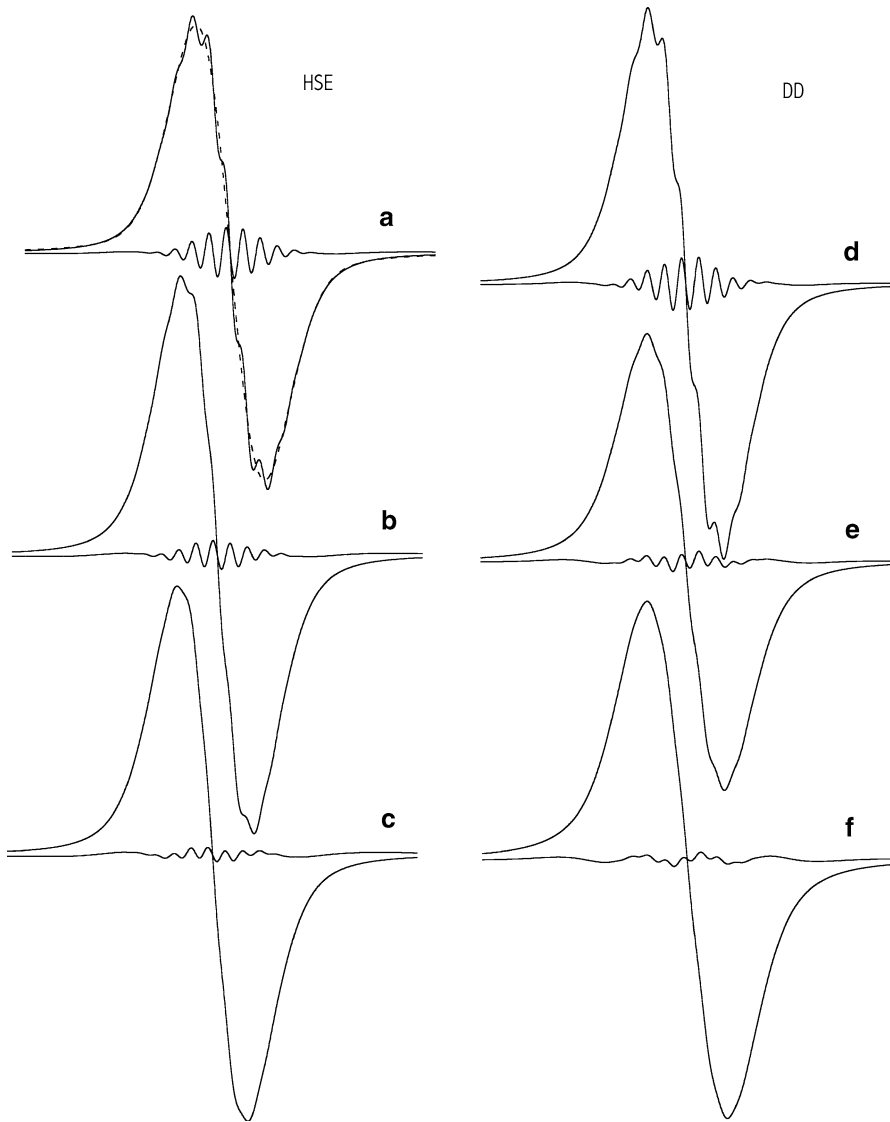
Fig. 19 Spectra for the lf-manifold only computed from Eq. (1) for a ^{15}N nitroxide, $A_0 = 22$ G with hyperfine coupling to 12 equivalent protons, $a = 0.4$ G, with $K_{ex}C/\gamma = $ **a** 0.03 G, **b** 0.06 G, **c** 0.09 G; or with $W_{dd}C/\gamma = $ **d** 0.0525 G, **e** 0.1575 G, **f** 0.2625 G. $\Delta H_{pplf}^L(0) = 0.45$ G. The spectra were fit with Eq. (44) and the residuals computed. The smaller trace overlying each spectrum shows the residual. The fit is shown only for **a** in order not to obscure the distortions in the other spectra that are evident near the peaks of **b–e**. A practiced eye will also detect distortions in **f**
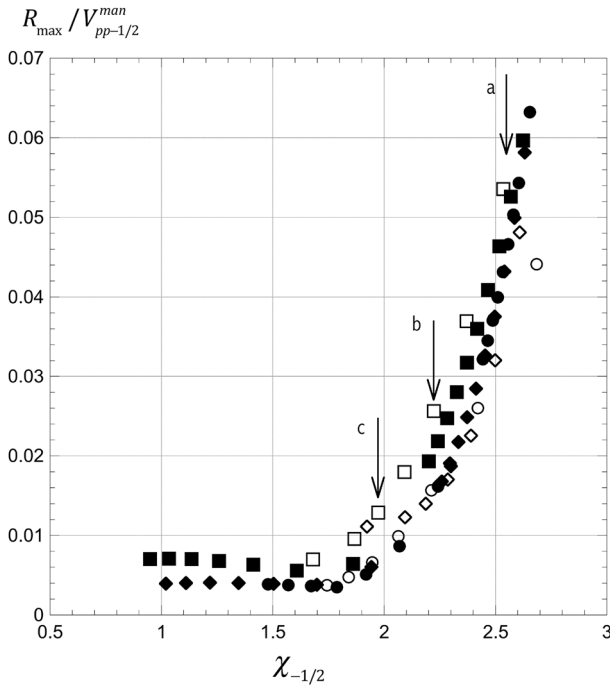
Fig. 20 Maximum value of the residuals, R_{max}, as a fraction of $V_{-1/2}^{man}$ from fits to Eq. (44). Diamonds, DD; squares, HSE; circles $C = 0$. Open symbols, $a = 0.2$ G; closed, $a = 0.4$ G. The vertical arrows indicate values of $\chi_{-1/2}$ corresponding to spectra in Fig. 19a–f, respectively

$\Delta H_{ppM}^{L}(0) = 0.69$ G, $R_{max}/V_{lf}^{man} < 0.004$ for HSE, DD, and $C = 0$, all having $\chi_{lf} < 1.9$ and showing no hint of incipient resolution.

One question is how well does the Voigt model IHB spectra; another, just as important, is how well do the fit parameters compare with the known input parameters. This can only be done for $C = 0$ spectra because we do not know the input values except there. In Fig. 21 this question is addressed over the range of $\chi_{-1/2}$ in Fig. 20 and higher, where input and fit values of line widths of $C = 0$ spectra are displayed. The solid squares are input values of $\langle \Delta H_{ppM}^{L} \rangle$ and the open squares, the fit values of $\Delta H_{ppM}^{L(Voigt)}$. The solid circles show input values of $\Delta H_{ppM}^{G(Voigt)} = a\sqrt{\alpha N}$, from Eq. (8), and the open squares, the fit values of $\Delta H_{ppM}^{G(Voigt)}$. The vertical arrows indicate values of χ_{lf} corresponding to the spectra in Fig. 19a, b, respectively. The inset shows the spectrum and residuals for the $\chi_{M} = 2.85$; compare with Fig. 19a, b, respectively. It is clear that excellent accuracy is obtained in support of Assumption 1, even for spectra that are clearly partially resolved. This interesting fact holds for spectra showing considerably more resolution that in the inset; however, detailed investigation is outside the scope of this paper.
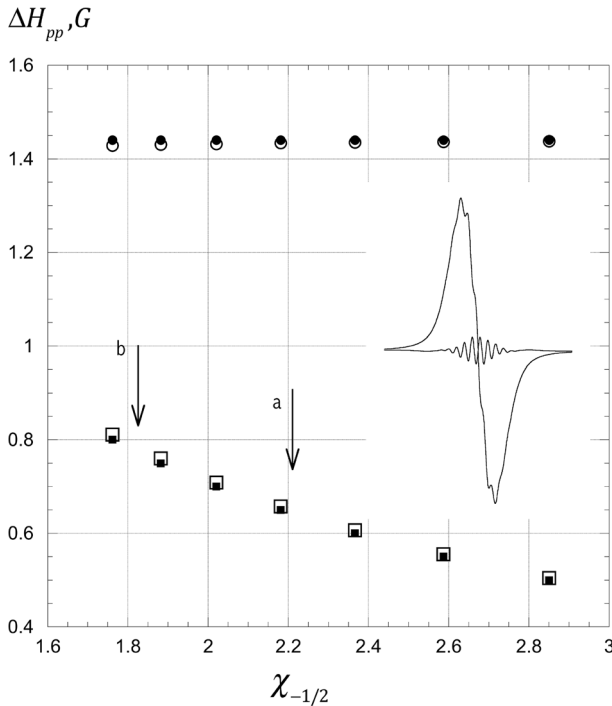
Fig. 21 Input and fit values of line widths of $C = 0$ spectra. Solid squares, input values of $\langle \Delta H_{ppM}^{L} \rangle$ and open squares, fit values of $\Delta H_{ppM}^{L(Voigt)}$. Solid circles, input values of $\Delta H_{ppM}^{G(Voigt)} = a\sqrt{\alpha N}$, from Eq. (8), and open squares, fit values of $\Delta H_{ppM}^{G(Voigt)}$. The vertical arrows indicate values of $\chi_{-1/2}$ corresponding to two of the spectra in Fig. 19a, b, respectively. The inset shows the spectrum and residuals for the $\chi_M = 2.85$; compare with Fig. 19a, b, respectively

Appendix 3: The Reason that the *p*-Parameter is in Error for the Low-Field Line of 14 NH at 273 K

Figure 22 shows values of $-p_{lf}A_0/3$ and $+p_{hf}A_0/3$ for 14 NH at 273 K taken from Fig. 11b on a larger scale. We observe that, while the hf results are reasonably linear, the lf results are not.

Figure 23 shows a spectrum at 273 K together with the residual, which shows an impurity line overlapping the main spectrum in the vicinity of the measurement of $p(lf)$. The impurity does not appear to amount to much on this scale, but because the asymmetry is so small, it makes a large difference in the *p*-parameter. Clearly there is no significant extraneous line for the high-field line so it's not affected.

Note also that for the cf and hf-manifolds where interference due to extraneous lines is not severe, the line shape is an excellent Voigt as shown by the small residuals.
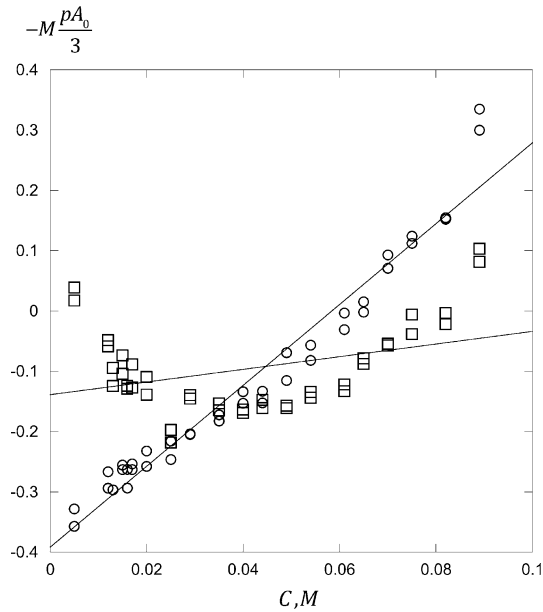
Fig. 22 Values of $-p(\mathrm{lf})A_0/3$ (squares) and $p(\mathrm{hf})A_0/3$ (circles) for 14NH at 273 K shown here on a larger scale than in Fig. 11b. The straight lines are linear fits, showing that the hf results are reasonably linear; however, the lf results are not
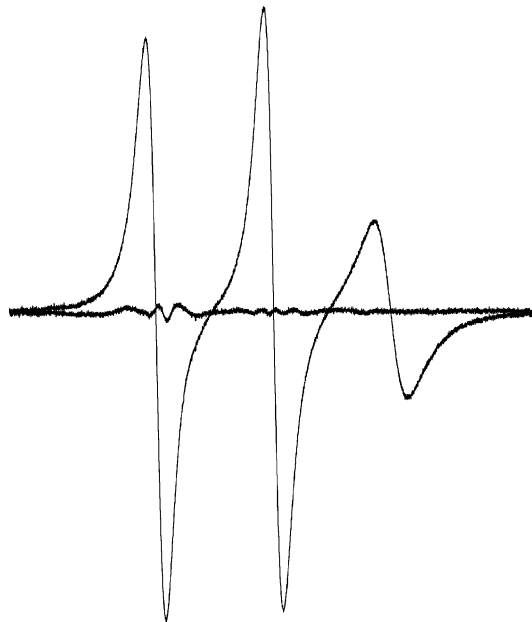

Fig. 23 EPR spectrum of 10-mM 14 NH at 273 K together with the residual where an impurity line is evident in the lf-manifold

References

1. K.H. Hausser, Z. Naturforsch. **14a**, 425 (1959)
2. G.E. Pake, T.R. Tuttle Jr., Phys. Rev. Lett. **3**, 423 (1959)
3. D. Kivelson, J. Chem. Phys. **33**, 1094–1106 (1960)
4. J.D. Currin, Phys. Rev. **126**, 1995 (1962)
5. K.M. Salikhov, Appl. Magn. Reson. **47**, 1207–1227 (2016) **(published online 24 September 2016)**
6. B.L. Bales, M. Peric, J. Phys. Chem. B **101**, 8707–8716 (1997)
7. Y.N. Molin, K.M. Salikhov, K.I. Zamaraev, *Spin Exchange. Principles and Applications in Chemistry and Biology* (Springer, New York, 1980)
8. L.J. Berliner, *Spin Labeling: Theory and Applications* (Academic Press, New York, 1976)
9. L.J. Berliner, *Spin Labeling II: Theory and Applications* (Academic Press, New York, 1979)
10. L.J. Berliner, *Spin Labeling: Theory and Applications* (Plenum Publishing Corporation, New York, 1989)
11. B.L. Bales, M. Meyer, S. Smith, M. Peric, J. Phys. Chem. A **113**, 4930–4940 (2009)
12. B. Berner, D. Kivelson, J. Phys. Chem. **83**, 1406 (1979)
13. B.L. Bales, M. Peric, Appl. Magn. Reson. **48**, 175–200 (2017)
14. K.M. Salikhov, Appl. Magn. Reson. **38**, 237–256 (2010)
15. K.M. Salikhov, A.G. Semenov, Y.D. Tsvetkov, *Electron Spin Echo and its Application* (Nauka, Novosibirsk, 1976). **(in Russian)**
16. A. Abragam, *Principles of Nuclear Magnetism* (Oxford University Press, London, 1986)
17. K.M. Salikhov, M.M. Bakirov, R.T. Galeev, Appl. Magn. Reson. **47**, 1095–1122 (2016)
18. B.L. Bales, M. Meyer, M. Peric, J. Phys. Chem. A **118**, 6154–6162 (2014)
19. B.L. Bales, D. Willett, J. Chem. Phys. **80**, 2997–3004 (1984)
20. B.L. Bales, in *Biological Magnetic Resonance*, ed. by L.J. Berliner, J. Reuben (Plenum, New York, 1989)
21. K.M. Salikhov, J. Magn. Reson. **63**, 271–279 (1985)
22. H.J. Halpern, M. Peric, C. Yu, B.L. Bales, J. Magn. Reson. **103**, 13–22 (1993)
23. B.L. Bales, Cell. Biochem. Biophys. (2016). doi:10.1007/s12013-016-0760-7
24. S.N. Dobryakov, Y.S. Lebedev, Sov. Phys. Dokl. **13**, 873 (1969)
25. B.L. Bales, M. Peric, J. Phys. Chem. A **106**, 4846–4854 (2002)
26. B.L. Bales, M. Peric, I. Dragutan, J. Phys. Chem. A **107**, 9086–9098 (2003)
27. B.L. Bales, F.L. Harris, M. Peric, M. Peric, J. Phys. Chem. A **113**, 9295–9303 (2009)
28. B.L. Bales, K.M. Cadman, M. Peric, R.N. Schwartz, M. Peric, J. Phys. Chem. A **115**, 10903–10910 (2011)
29. B.L. Bales, M. Meyer, S. Smith, M. Peric, J. Phys. Chem. A **112**, 2177–2181 (2008)
30. M.R. Kurban, M. Peric, B.L. Bales, J. Chem. Phys. **129**, 064501-1–064501-10 (2008)
31. I. Peric, D. Merunka, B.L. Bales, M. Peric, J. Phys. Chem. B **118**, 7128–7135 (2014)
32. K. Yamada, Y. Kinoshita, T. Yamasaki, H. Sadasue, F. Mito, M. Nagai, S. Matsumoto, M. Aso, H. Suemuni, K. Sakai, H. Utsumi, Arch. Pharm. Chem. Life Sci. **341**, 548–553 (2008)
33. J. Pirrwitz, D. Schwarz, DDR Patent, 222017 A1 (WP C 07 D/260 901 6)
34. L.A. Shundrin, I.A. Kirilyuk, I.A. Grigor'ev, Mendeleev Commun. **24**, 298–300 (2014)
35. D. Marsh, J. Magn. Reson. **277**, 86–94 (2017)
36. K.M. Salikhov, A.Y. Mambetov, M.M. Bakirov, I.T. Khairuzhdinov, R.T. Galeev, R.B. Zaripov, B.L. Bales, Appl. Magn. Reson. **45**, 911–940 (2014)